POLITECNICO DI TORINO
Repository ISTITUZIONALE

An automotive steel wheel digital twin for failure identification under accelerated fatigue tests

(Article begins on next page)

01 September 2025

An automotive steel wheel digital twin for failure identification under accelerated fatigue tests

Simone Venturini *, Carlo Rosso, Mauro Velardocchia

Department of Mechanical and Aerospace Engineering, Politecnico di Torino, Corso Duca degli Abruzzi, 24, Torino, 10129, Italy

ARTICLE INFO

ABSTRACT

In this paper, a digital twin to predict failure in automotive steel wheels during experimental fatigue tests is proposed. The methodology involves a wheel finite element model that incorporates assembling and mounting processes, and CDTire/3D simulation package, employed to calculate tyre to rim generalised internal forces in several loading conditions. The two models are decoupled under small deformation assumption, which allows to reduce computational effort for batch simulations. The Digital Twin (DT) is designed to meet the standard requirements and the working principles of test benches for dynamic cornering, radial, and biaxial fatigue tests. The overall DT architecture is described with emphasis on different test bench logic and the introduction of simplifications to efficiently estimate failure under mean stress variation. Then, a simplified formulation of the critical plane McDiarmid multi-axial failure criterion is presented to face the non-proportionality of stress path under loading conditions. Finally, the methodology is validated against an industrial case study: the predicted failures are compared to experimental test result database for wheel topologies, material properties, test benches and loading conditions.

1. Introduction

The wheel behaviour is decisive to the vehicle performance. Wheels must be designed to meet the vehicle structural requirements because they make a substantial contribution to numerous essential functions, e.g., the transferal of the generalised forces from the axle to the tyre, the support of impact forces from the road and the weight of the vehicle, the driving stability, the safety, and the comfort [1–3].

Therefore, the design of wheels must meet several regulatory standards aspects i.e., dimensional uniformity, material compliance, and testing requisites for wheel reliability. In Europe, the dimensional uniformity and material compliance regulations are harmonised by the ISO 3894:2023 standard [4], the European Tyre and Rim Technical Organisation (ETRTO) [5] and the Association of European Wheel Manufacturers (EUWA).

Technical standards establish experimental accelerated fatigue tests to ensure the reliability of wheel performance. These tests include dynamic cornering (DCFT), radial (RFT), and biaxial (BFT) fatigue tests. Focusing on passenger cars and light trucks, SAE J328 [6] outlines the requirements for DCFT and RFT. Back in 1980s, Fraunhofer LBF introduced a methodology and equipment for conducting BFT on vehicular tyres and wheels. This innovative approach, lately known as ZWeiAchsige RadPrüfung (ZWARP), involves continuously monitoring camber angle during operational conditions, allowing for tailored accelerated fatigue tests which better represent the entire lifespan loading conditions compared to previous test procedures. As a result, in 2003, SAE J2562 [7]

Nomenclature

Wheel behaviour and test-rig functionality

b	DCFT test bench arm (m)
ET	Wheel inset (ISO 3911:2021) (m)
r_l	BFT tyre loaded radius (m)
ε	DCFT seismic mass eccentricity (m)
β	RFT slip angle (rad)
ω	Angular velocity (rad/s)
m	DCFT seismic mass (kg)
μ	Tyre-road friction coefficient (–)
n_b	Number of bolt holes (–)
t	Wheel laminate thickness (–)
S	DCFT accelerated scale factor (–)
T_b	Average bolt tightening torque (N m)
p	Nominal inflation pressure (Pa)

Digital twin properties

α_w	Angular position of wheel rim node around revolution axis (rad)
δ	Wheel force field rotation angle (rad)
r_w	Rim flange circle of action radius (m)
$\tilde{\mathbf{F}}_t, \tilde{\mathbf{T}}_t$	Generalised tyre sidewall force field (N, N m)
$\tilde{\mathbf{F}}_w, \tilde{\mathbf{T}}_w$	Generalised rim flange force field (N, N m)

Material properties and stress analysis

D, DF	Non-dimensional damage factor (–)
K	Simplified Wöhler curve slope coefficient (–)
n_c	Number of load regimes (–)
n_l	Number of evaluated layers (–)
N	Number of life cycles to failure in load regime (–)
N_{rW}	Minimum requirement number of cycles to failure (–)
φ, θ, ψ	Rotation matrix angles (rad)
$\mathbf{R}$	Rotation matrix (–)
$\mathcal{R}(\mathbf{u}, \mathbf{v}, \mathbf{w})$	Layer stress tensor reference frame (–)
$\mathcal{R}(\mathbf{x}, \mathbf{y}, \mathbf{z})$	Direct stress tensor reference frame (–)
E	Young modulus of elasticity (GPa)
$\boldsymbol{\sigma}$	Direct stress tensor (MPa)
$\sigma_{a,eq}$	Equivalent fully reversible alternate stress (MPa)
σ_l	Layer stress (MPa)
$\sigma_{n,\max}$	Maximum normal stress (MPa)
σ_{R-1}	Tensile fatigue limit for fully reversible tension (MPa)
σ_{UTS}	Ultimate tensile strength of material (MPa)
σ_Y	Yield strength of material (MPa)
$\tau_{a,l}$	Layer alternate shear (MPa)
$\tau_{a,\max}$	Maximum alternate tangential shear (MPa)
$\tau_{f_{A,B}}$	Shear fatigue limit for Irwin mode A and B (MPa)
τ_{R-1}	Shear fatigue limit for fully reversible torsion (MPa)

introduced a wheel standard with additional specifications for newly introduced BFT configurations. Furthermore, EUWA ES-3.23 introduced BFT standards for truck wheels [8].

Meeting technical standard requirements through experimental testing can lead to rising production costs. The conventional wheel design involves development and prototype testing in a continuous iterative process. In testing, strain gauges are strategically placed near the crack nucleation sites on the wheel to measure local strain. The crack nucleation sites are identified in previous experiments. Careful adjustments are needed to prevent premature strain gauge fatigue failures during testing.

The integration of virtual simulation in automotive design streamlines the iterative process, reducing resource consumption. However, numerical models have limitations, tailored to specific behaviours. Enhancing the numerical model reliability requires addressing the overall industrial process variability, with random checks to meet project tolerances i.e., geometric tolerances must be considered during component design for in-service conditions. Also, manufacturing uncertainties impacts structural property variability, as seen in high-density natural frequency measurements on a bike spoke wheel [9] and a benchmark for wheel press-fit identification [10]. This poses challenges for wheel producers seeking accurate virtual simulations.

The growing demand for shorter component development times in the automotive industry have led to the widespread integration of Digital Twin (DT) paradigm. A DT is a virtual replica or representation of a physical object, system, or process. It encompasses a combination of simulation, modelling techniques, and real system data to create a comprehensive digital counterpart that mirrors the characteristics, behaviour, and attributes of its physical counterpart. DT enable analysis, optimisation, and eventually real-time monitoring of physical assets and processes, offering valuable insights for decision-making, predictive maintenance, performance optimisation, and design improvements [11,12]. The DT paradigm covers a wide set of models and applications, in which several features are emphasised, mainly depending on the entity to be modelled, and the level of interaction expected. Recently, Semeraro et al. highlighted the presence of five different DT clusters, focusing on production, physical systems, modelling, simulation, and life cycle [13]. In [14], it is presented a brief investigation of the FE-based DT in the state-of-the-art which highlighted the common application in automotive field for monitoring, virtual sensing, and process monitoring. [15]. In 2019, Biesinger et al. highlighted the need for DT development in automotive industry, offering implementation guidelines [16]. The automotive sector has increasingly embraced DT for applications such as virtual sensing, homologation, and process simulation, including a virtual sensor for wheel angular position considering sensor uncertainties [17] and aircraft tyre touchdown diagnosis based on uncertain parameters [18]. Researchers have also utilised DT for estimating fuel consumption variability [19] and structural analysis and Structural Health Monitoring (SHM) [20,21]. Real-time DTs have been developed for electric vehicle motor prognostics [22], while automotive braking systems have seen DTs coupling various modelling techniques for brake pad wear estimation [23,24]. Additionally, a process-based DT for automotive steel wheel flow forming process was developed and validated using digital photogrammetry [25], demonstrating the relevance of finite element (FE) models in process-related DT applications, offering faster and cost-effective alternatives to physical experiments.

The development of DT of automotive steel wheel behaviour under fatigue tests requires the stress analysis of the whole wheel. Also, fatigue behaviour depends on wheel mean and alternate stress distribution which eventually depends by the tyre–wheel interaction. The wheel flexibility must be considered in the modelling phase and FE technique is globally accepted to describe stress distribution. Instead, a more complex situation is related to the tyre–wheel interaction.

Several tyre models are available in the state of the art and the market, catering to different needs and applications:

- Semi-empirical models as MF-Tyre and MF-SWIFT [26] which lack the capability to provide wheel rim flange force distributions. The latter offers accurate steady-state and transient behaviour up to 100 Hz. MF-SWIFT utilises a 6-Degree Of Freedom (DOF) rigid ring representing the tyre belt, coupled with lumped springs and dampers to a rigid wheel. However, it cannot describe flexible tyre modes but incorporates elliptical cam contributions for terrain interaction.
- Semi-analytical models such as [27,28] depict the physical nature of sidewall flexural contributions, allowing for reliable force distribution among rim flanges, primarily under radial loading conditions.
- cosin FTire [29], designed for dynamic behaviour up to 150 Hz, focuses on vehicle dynamics and assumes an infinitely rigid wheel. It is a 3D model that considers tyre belt behaviour for handling, comfort, and Noise, Vibration and Harshness (NVH).
- cosin FTire/rim [30] extends these capabilities by monitoring rim reactions and offering stress analysis functionalities.
- Fraunhofer CDTire [31] simulation package is tailored for handling, comfort, and durability simulations.
- Fraunhofer CDTire/3D [32] and LBF WheelStrength [33] are focused on wheel stress analysis and durability. These last two employ Finite Difference (FD) shell elements calibrated to material properties for tyre modelling, and are primarily focused on alloy wheels without considering tightening torque on bolts and assembling residual stresses.

In the market, leading software for wheel simulation prioritises tyre-oriented aspects, such as handling and NVH behaviours, assuming wheel as rigid body. This assumption is justified since the passenger car tyre relevant NVH bandwidth is within 120÷140 Hz, whereas classic steel and aluminium alloy wheel first natural frequency range is 200 ÷ 500 Hz. Additionally, obtaining wheel rim flange force distributions is generally impractical from semi-empirical or vehicle dynamics-related tyre models. Therefore, the wheel durability assessment can be approached using semi-analytical [27,28] or physical [30,32] models.

In order to perform the wheel durability assessment, it is necessary to investigate the stress distribution causes occurring in the wheel production process. Specifically, the automotive steel wheel i.e., the assembly obtained by press-fit of the disc and the rim components, is subject to residual stresses and pre-stress [1]. Differently from the cast aluminium alloy wheels, in which the residual stress is caused by thermal gradients and inadequate shrinkage in solidification and inhomogeneity of microstructure and microdefects [34,35], the steel wheel residual stress is due to component plastic deformations during the production process:

- Disc and rim forming and coining processes inducing plastic deformation.
- Disc-rim interference fit.
- Disc-rim welding [36].

Instead, the following mechanisms are external stress causes, inducing pre-stresses:

- Disc hub bolt tightening.

Table 1
Accelerated fatigue tests. State-of-the-art summary.

Research	Residual/ Pre-stress	DCFT	RFT	BFT
MF-Tyre, MF-SWIFT [26]	–/–	–	–	–
FTire/rim [30]	–/✓*	–	–	–
Ballo et al. 2018 [28]	–/✓*	–	✓*	–
CDTire/3D [32]	–/✓*	–	–	–
WheelStrength [33]	–/✓	✓*	✓*	✓*
Zheng et al. 2014 [39]	–/–	✓	–	–
Shang et al. 2016 [40]	✓*/–	✓	–	–
Zhao et al. 2017 [41]	–/✓*	–	✓*	–
Bonisoli et al. 2020 [43]	✓*/✓	–	✓	–
Zanchini et al. 2023 [44]	–/✓*	✓	✓	–
Duan et al. 2021 [35]	✓/–	–	–	✓
Wan et al. 2016 [46]	–/✓*	–	–	✓
Santiciolli et al. 2017 [45]	–/–	–	–	✓*
Ballo et al. 2020 [47]	–/✓*	–	–	✓
Current work	✓*/✓	✓	✓	✓

- Tyre-rim axial/radial fitting.
- Tyre inflation pressure.
- Testing conditions.

Therefore, a precise material selection has to be considered to improve the wheel fatigue life, as Mazzoni and Solazzi demonstrated by in-situ experimental tests on a multipiece steel wheel [36]. In [37], a complete investigation of all the adopted experimental test procedures in wheel design validation is performed and simulation guidelines are suggested. In [38], the authors investigated the three fatigue tests to develop a simulation framework embedding wheel main stress distribution causes. The authors validated the framework against a limited set of loading conditions for RFT and BFT with stress analysis.

In [39] the DCFT has been simulated with wheel FE models ignoring the pre-stress induced by disc and rim interference fit. In [40], Shang et al. introduced forming residual stress in the FE simulation showing a marginal contribution to the fatigue assessment, even though the interference fit and the bolt tightening are not considered.

The RFT simulation is generally computed with a simplified description of the wheel rim flange load profile instead of using physical tyre models. In [41,42] the RFT load profile is modelled with cosine function model. Additionally, [42] adopted pressure matrix sensors to calibrate the model on the inner and outer wheel rim flanges. The usage of physical tyre models allow to effectively apply for non-null slip angle loading conditions in which cosine model is not consistent. In [43], the authors adopted CDTire/3D to introduce wheel rim flange load. The steel wheel FE model considers main residual and pre-stress mechanisms such as interference fit and wheel–tyre interaction. Also, in [44] the RFT load profile is caused by the mutual interaction of wheel and tyre FE model and used to effectively perform a comparative fatigue analysis on aluminium and composite wheels for sport cars. The developed simulation environment considers all pre-stress causes but bolt tightening torque.

The BFT definitely limited the application of simplified load models since the loading conditions and drum geometry require to consider large tyre deformations. Santiciolli et al. [45] used CDTire simulation package to compute the wheel rim overall generalised forces induced by loading conditions. Different multibody co-simulation schemes are introduced to evaluate the overall wheel flexibility, showing interesting results for BFT EUWA ES-3.23 requirements. In [46,47], an hyper-elastic Money–Rivlin tyre FE model is coupled with the wheel. The static deformation of the tyre induced by vertical load and imposed camber angle are used for fatigue assessment. More recently, Duan et al. performed BFT on a A356 cast aluminium alloy introducing shrinkage and microcavities effect in the physical experiment. The result is an efficient BFT virtual experiment. Nevertheless, it lacks of full pre-stress mapping and versatile depiction of DCFT and RFT [35].

Also, random excitation and in-situ experimental activity is adopted for high performance vehicle applications and for heavy vehicles. In [48] the high cycle fatigue life of an automotive component is virtually estimated by using a multibody vehicle model. Instead, in wheel [49] random fatigue in time and frequencies domain is experimentally and analytically studied on an industrial alloy wheel, showing influence of microdefects in fatigue life.

The limitations of the state-of-the-art are multiple. Table 1 summarises the analysis performed in the previous paragraph. The "✓" symbol refers to full coverage of the feature, while "-" symbol means the feature is completely absent, instead "✓*" symbol means the feature is not completely covered by the methodology. The residual stress is never completely described: in [40] the vertical and horizontal loads and stamping production process are reported, but the disc-rim fitting is not considered. Also, pre-stress is usually missing bolt tightening torque, which is consistently implemented only in solutions supplied by the authors [43]. Eventually, also wheel–tyre axial fit is neglected in RFT simulations based on cosine function models [41]. There are not simulation procedures which are versatile enough to be generically applicable for different loading conditions. Moreover, researches focused on BFT [46,47] adopt custom tyre FE models with material properties which are usually not available at wheel manufacturers. The whole wheel–tyre simulation is performed together, increasing computational costs.

Therefore, the objective of this paper is to present a developed reliable and versatile DT for automotive steel wheel fatigue tests (see the last row of Table 1). The presented model satisfies the basic requirements of DT of C1 cluster [13]. The developed DT
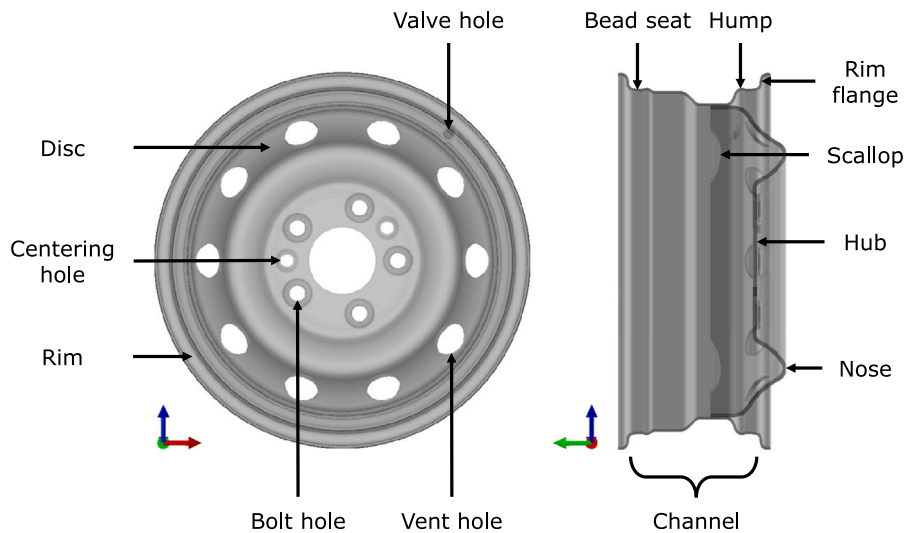
Fig. 1. Automotive steel wheel terminology.

embeds decoupled FE tyre model simulations in time domain and wheel FE model static simulations. Without loss of generality, the FE tyre model is implemented with CDTire/3D package. The decoupling allows to drastically reduce computational costs for batch simulations and to store tyre mark simulations during the wheel design process. The presented DT architecture allows to easily introduce residual stress and pre-stress mechanisms on wheel. A multi-axial fatigue criterion for non-proportional stress path [50] is selected and modified to reduce the computational cost. The developed DT is deeply validated against experimental fatigue database of several wheel topologies in DCFT, RFT, and BFT scenarios for different loading conditions.

The following paperwork is divided in six sections.

In Section 2 the adopted terminology and nomenclature is presented.

In Section 3 the working principles of DCFT, RFT, and BFT test benches are described.

In Section 4 the proposed DT architecture is depicted: the main aspects of wheel and tyre decoupling are developed and the integration with CDTire/3D simulation package is approached. Moreover, modified versions of McDiarmid failure criterion [51] and Palmgren–Miner cumulative damage [52] are described.

In Section 5 the validation is performed on a wide industrial case study: 12 wheel geometries concerning three different wheel topologies are studied with the developed DT against 24 different loading conditions in DCFT, RFT, and BFT: the fatigue life and the damage distribution are compared with experimental tests database evidence as the sensitivity of damage to certain geometrical features such as disc scallop.

Finally, Section 6 is dedicated to conclusive thoughts.

2. Terminology and nomenclature

In this section, the terminology related to the wheel and tyre, and the nomenclature of all quantities defined and adopted in the proposed methodology are presented. The terminology refers to ISO 3911-2021 standard [53] which is summarised in Fig. 1.

Fig. 1 shows the main components of the automotive steel wheel, or wheel, and the terminology of the component regions and features approached in the next sections. In the following paper the disc inner surface is intended to be the surface of the formed metal which is facing the brake system in a vehicle, while the rim inner surface is the surface of the hot rolled metal plate which is in contact with the inflated pressure volume and the tyre.

A nomenclature box lists all the quantities used for the formulation of the procedures used in the developed DT. The nomenclature box is not related to quantities defined in Appendix. Also, the generalised forces acting on the rim flanges are represented in two different established reference frames [54].

A detailed description of the adopted tyre terminology and nomenclature can be found in [14].

3. Experimental test benches

This section describes the main characteristics of experimental fatigue test procedures and corresponding hardware. The procedures follow consolidated standards such as ISO 3894:2023 [4], SAE J328 [6], and SAE J2562 [7]. The standards focus on characteristics of the fixture, loading conditions, and stop conditions for fatigue failure.
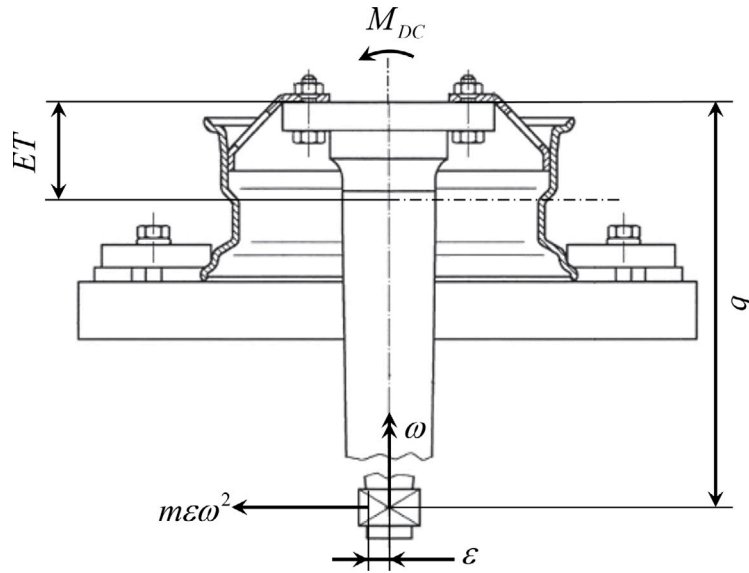
Fig. 2. DCFT bottom clamping fixture and rotating bending moment scheme [4].

3.1. Dynamic cornering fatigue test

The DCFT applies a constant rotating bending moment to the wheel hub while the inner flange is clamped to a fixed hub. Fig. 2 shows the bottom clamping method established in [4]. During the test, the rotating bending moment is applied on the disc hub by a slender arm. Standards supply different mechanisms to generate the exciting load: ISO 3894:2023 [4] applies a constant load parallel to the fixture plane on the extremity of an arm. Hence, the whole fixture and wheel are brought to rotation. Instead, SAE J328 [6] generates the dynamic cornering moment by rotating an eccentric mass hinged to the main arm tip in synchronous forward whirl mode (Fig. 2).

Therefore, the dynamic cornering moment amplitude depends on the rotor angular speed. The dynamic cornering moment M_{DC} acting on the wheel hub is obtained by:

$$M_{DC} = S \left(\mu \, r_{l,\max} + ET \right) F_{Z_W,\max} = bm\varepsilon\omega^2 \tag{1}$$

where μ is the assumed friction coefficient developed between tyre and road (0.7 for [4]), $r_{l,\max}$ is the largest value of the static loaded radius of the tyres which can be applied to the wheel or prescribed by the vehicle manufacturer, ET is the inset, i.e., positive offset of the wheel hub from the middle of the rim channel, F_{Z_W} is the maximum vertical static load. S is an acceleration test factor (from 1.1 to 1.6 for [4]).

The test-rig bending moment is obtained through a control loop based on strain measured by strain gauges in two orthogonal positions on the sender arm. When the measured strain is below a certain percentage of the rated strain, the wheel reached a consistent fatigue failure condition and the test is stopped.

3.2. Radial fatigue tests

The RFT evaluates the durability of the wheel under tyre rolling load condition, as it occurs on a road drive session. The wheel is driven by a rotating drum simulating the road contact with the tyre (Fig. 3).

The test machine imparts a constant radial load as the wheel rotates: the suggested rolling drum presents a smooth surface wider than the loaded test tyre section width. The mating surfaces of the test adaptor and wheel shall be free of excessive scoring and deformation and excessive build-up of paint, dirt, or foreign matter. The test wheel and tyre fixture shall provide loading normal to the drum's external surface. ISO and SAE standard prescribes inflation pressure and acceleration factors [4,6].

A control loop is based on the internal reactions measured by the wheel hub sensor. The wheel loaded radius depends on an initial radial static deformation of the tyre. The test-rig control logic starts with a preliminary phase in which the drum is locked, and the radial load is applied to the wheel by moving the hub; the sensor hub closes the loop and stops the loading when the target radial load is reached; the rolling radius is detected. The drum is started, and its angular speed is defined to obtain the requested tangential speed in the centre of the contact patch. The sensor hub measures internal reactions and considers them steady-state references for the test.
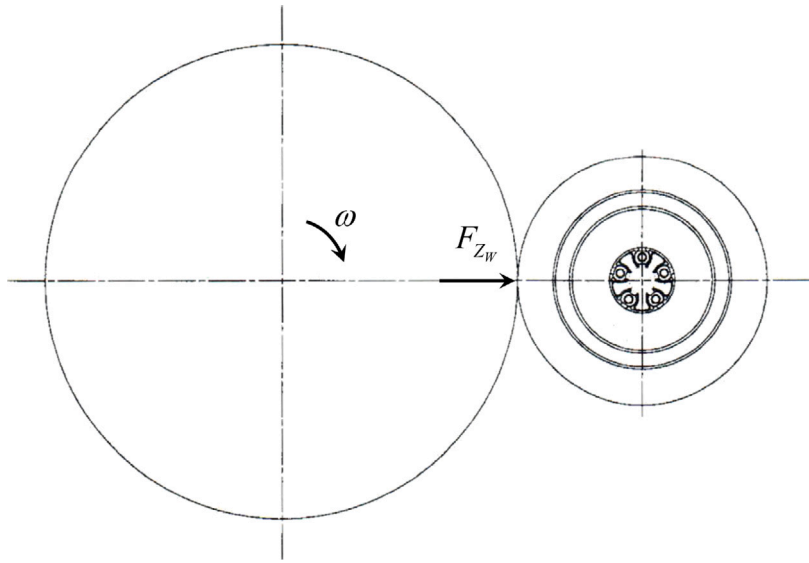
Fig. 3. RFT scheme [6].
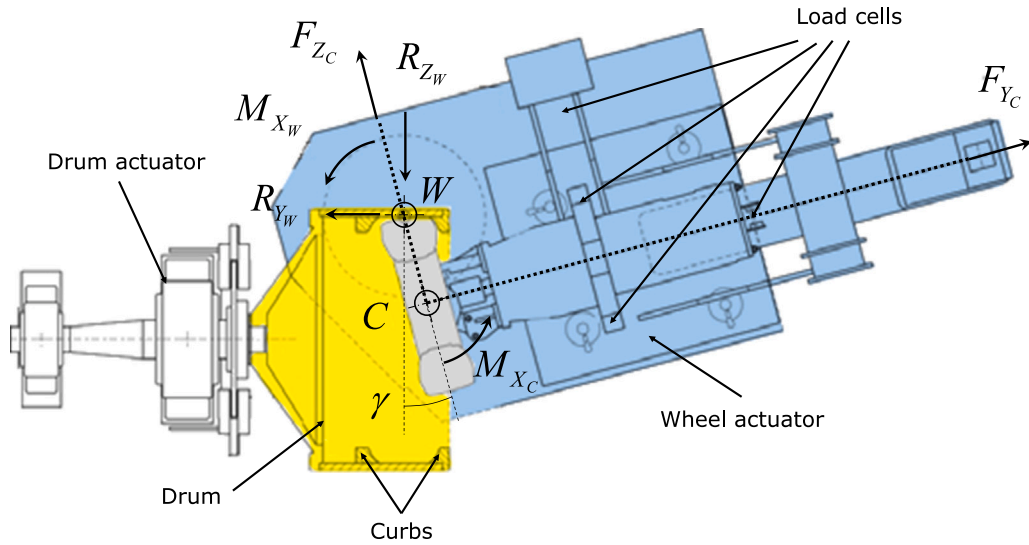
Fig. 4. BFT detailed cross-section of typical tyre–wheel assembly inside drum with inboard lateral load [7,55].

3.3. Biaxial fatigue tests

The BFT is the road-simulator able to apply radial and lateral loads dynamically vary them during the test. Conditions of acceleration and braking can also be reproduced within the test procedures. The apparatus helps to evaluate the fatigue resistance of the wheel in accelerated and repeatable conditions. The wheel is brought in contact with a rotating hollow drum. The drum presents a set of curbs on the lateral surfaces increasing the developed lateral load during operation (Fig. 4).

The test-rig logic requires a calibration procedure called Overturning Moment (OTM) procedure in which the γ_{OTM} for each vertical load F_{Z_C} and lateral load F_{Y_C} requirement is evaluated. The procedure is based on the following relation called OTM condition:

$$M_{X_W}\left(\gamma_{OTM}\right) = M_{X_C}\left(\gamma_{OTM}\right) - F_{Y_C}\, r_l\left(\gamma_{OTM}\right) = 0 \qquad (2)$$

where F_{Y_C} is the required lateral load in the BFT, $r_{l,start}$ is the loaded wheel radius and M_{X_C} is the overturning moment. Since, the wheel actuator defining the camber angle is coaxial with the centre of contact patch (Fig. 4), it is necessary to reach the equality between the overturning moment and the moment generated by lateral load to avoid resistant torque on the actuator shaft. In high

loading condition regimes, high resistant torque can damage the actuating system. Under generic loading conditions, the contact patch may be over the curbs, therefore, to satisfy the OTM condition, a proper camber angle γ_{OTM} must be identified for prescribed loading conditions. For example, if lateral load F_{Y_C} is imposed null, the Eq. (2) is satisfied only if M_{X_C} is null; that is possible if $\gamma_{OTM} = 0$ is prescribed. Therefore, the machine executes a triangular ramp manoeuvre in which γ is slowly increased in time from an initial guess to a greater than optimal γ_{OTM} value. During the OTM procedure, the overturning moment will eventually cross twice the M_{X_C} target: γ_{OTM} for the fatigue test is obtained by averaging the γs at the target's two intersections. The final BFT will occur at computed γ_{OTM} at required lateral and radial loads. The fatigue test is interrupted when lateral and vertical forces measured by load cells are below a threshold of the rated loads.

4. Digital twin architecture

In this section, a DT for steel wheel fatigue assessment is proposed. The FE technique is adopted for wheel modelling to perform wheel fatigue assessment. Similarly, the CDTire/3D physical tyre simulation package is adopted to obtain the rim flange load profile in loading conditions in which the tyre is present. The DT architecture is based on the following assumptions:

- the tyre bead region deformation is much smaller than the rest of the tyre. Therefore, the tyre sidewalls are assumed radially hinged and circumferentially pinned to an infinitely rigid rim, by neglecting the bead deformation.
- the tyre bead infill is jointed to the rim flanges. Therefore, a rigid wheel–tyre interface is introduced.
- all the loading conditions are evaluated only in steady-state conditions.
- wheel and tyre dynamic behaviours are negligible.

Under these assumptions, a decoupled tyre and simulation scheme, already used in limited operative conditions in [47], is generalised. In Fig. 5 is summarised the developed DT architecture, which is divided in four consecutive steps.

- *Loading conditions*: the rim flange loading conditions are computed. The calculation is analytical for DCFT, while CDTire/3D environment is adopted for RFT and BFT load cases.
- *Stressed wheel*: wheel FE model is used and residual stress and pre-stress are induced for all the mechanisms. The result is a FE model which presents a pre-stress mapping.
- *Batch static analysis*: the calculated loading conditions are applied to the stressed wheel FE model in different angular static conditions. Stress tensor path mapping is obtained for the whole FE model.
- *Damage calculation*: once the stress tensor map is evaluated, an equivalent stress condition is defined through a failure criterion and the cumulative damage criterion is adopted to perform fatigue analysis i.e., damage map, number of cycles to failure and safety factors.

The passage from step #1 to step #2 allows to drastically reduce computational resources. In fact, being tyre and wheel simulations fully decoupled, it is possible to store loading conditions and wheel pre-stress mapping and combine them for different validation requirements. The proposed DT approach is significantly effective during iterative design. The tyre characteristics and loading conditions are usually invariant, while wheel design parameters or even topology may differ. In this case, it is only necessary to perform steps #2, #3, and #4. The same approach can be used for sensitivity analysis or uncertainty quantification. Differently, in validation process, the pre-stress mapping remains invariant and only steps #1, #3, and #4 have to be performed.

4.1. Loading conditions

Depending on the type of experimental test to simulate, concentrated nodal loads are computed with different approaches. In case of DCFT, the concentrated load at first time step is a vertical force in axial direction analytically expressed as a fraction of input dynamic cornering moment M_{DC}:

$$F_{Y_{C,i}} = \frac{2M_{DC}}{r_w} \frac{1}{n_w} \sin \alpha_{w,i} \tag{3}$$

where:

- M_{DC} is the dynamic cornering moment;
- r_w is the rim flange circle of action radius;
- n_w is the number of nodes in the flange circle of action;
- $\alpha_{w,i}$ is the angular position of ith node on the flange circle of action.

Instead, in case of RFT and BFT, the concentrated loads are computed with CDTire/3D simulation environment.

CDTire/3D offers a physical tyre model based on FD shell element formulation [32]. All the tyre functional layers i.e., radial ply, tread plies and sidewall, are condensed in shell properties. Also, cord-reinforced layers include non-linear elastic characteristic for compression and tension regimes. The geometric formulation of the material behaviour allows very large deformations. The tread is modelled by a brush-type contact formulation, allowing for local stick–slip effects. The model features a strict separation between material and geometric properties with the inflation pressure applied correctly onto the inner-liner surface of the tyre.

The RFT and BFT test-rig components i.e., cylindrical drum and hollow drum with curbs, are modelled and simulated with a customised CDTire/3D toolbox named WheelTestRig (WTR), developed with Fraunhofer and adopted for the activity [43]. The tyre
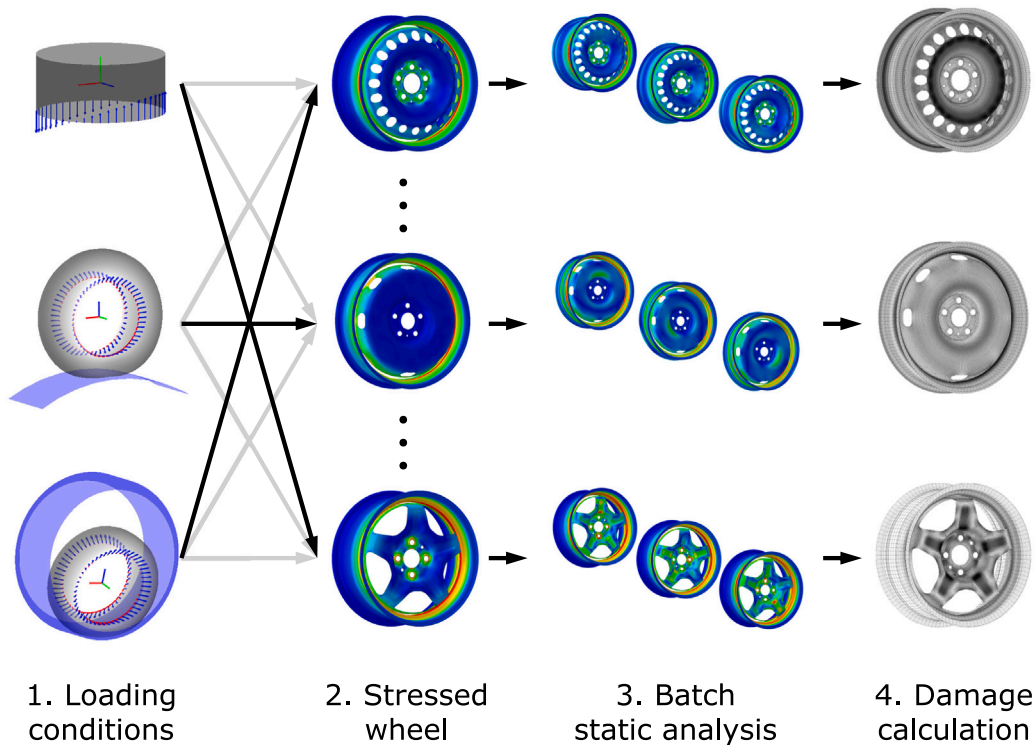
Fig. 5. DT architecture.

flexible body is hinged to a rigid wheel and the wheel centre is kinematically driven against rigid drum, while target vertical and lateral forces are imposed. The simulations are performed in time domain by direct integration scheme. Figs. 6 and 7 show three examples of WTR results for RFT and BFT load cases. Further details on the specifications of the load cases can be found in Section 5. In Fig. 6 the WTR simulation results are shown: the time domain evolution of the controlled and driven significant quantities are shown.

In case of RFT, the tyre in default condition i.e., not in contact with the drum and with $\beta = 0$ and $\gamma = 0$, is brought in contact with the rolling drum. Vertical load F_{Z_C} is imposed, while slip angle β is controlled until target lateral load F_{Y_C} is obtained. Fig. 6(a) shows an example of RFT manoeuvre with $F_{Y_C} = 0$ requirement. $\beta = 0$ is the resulting kinematic condition guaranteeing the prescribed lateral load. Instead, Fig. 6(b) shows an example of RFT manoeuvre with $F_{Y_C} > 0$ requirement. β is controlled until the prescribed lateral load is obtained.

In case of BFT, the preload is again measured and controlled in TC reference frame, but the lateral force F_{Y_C} is now controlled via a lateral displacement. This is possible because the inner drum presents curbs on which the tyre can enter in contact for gaining lateral support. The sidewall–curb interaction leads to non-linear variation of overturning moment M_{X_C}, which is remedied by controlling the camber angle γ until the target M_{X_C} is obtained. Fig. 6(c) shows an example of BFT manoeuvre in which γ_{OTM} is gradually reached by a linear ramp up to steady-state condition. Generalised forces F_{Y_C}, F_{Z_C} and M_{X_C} reach the prescribed values.

Then, the tyre generalised reaction force field ($\bar{\mathbf{F}}_t$ reaction force field and $\bar{\mathbf{T}}_t$ reaction moment field) is extrapolated from the last stable steady-state condition of the corresponding scenario. WTR supplies tyre $\bar{\mathbf{F}}_t$ and $\bar{\mathbf{T}}_t$ acting on two circular crowns of discrete positions representing the locations of hinge boundary condition to the rigid rim flanges.

In Fig. 7 the resulting steady-state condition load profile are shown. On the left side, is shown the angular distribution of radial force F_R, axial load F_L, and circumferential moment T_C following the sign convention indicated in the pictures and TC reference frame i.e., Y_C clockwise rotation starting from Z_C. The generalised forces are distinguished in "+" outer and "-" inner flange of action. On the right side, the graphical representation of the generalised forces is shown, in which blue vectors are forces and red ones moments. Fig. 7(a) shows that load profile is perfectly identical on inner and outer flanges. Moreover, the result is compliant with experimental load distributions in [42] and simulated ones in [28]. Differently, Fig. 7(b) shows non symmetric behaviour for $\beta \neq 0$ load case. The distribution is no more symmetrical among π location, since also the contact patch is shifted back longitudinally. Consequently, also moment reaction is greater on the side of the contact patch slide, while almost negligible on the other one. Finally, Fig. 7(c) shows a complex BFT load profile case. The distributions are almost symmetrical among π location, since low longitudinal force, but the outer and inner moments are also opposite in sign. The result is affected by the non-linear contact state between the tyre and the drum and curbs.
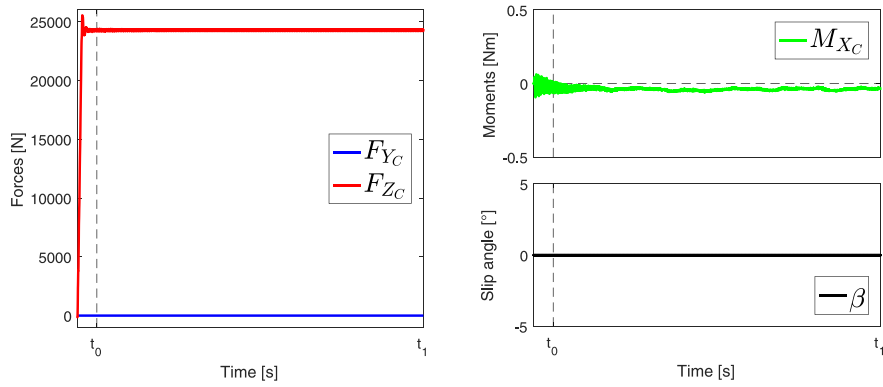
(a) RFT load case #2.
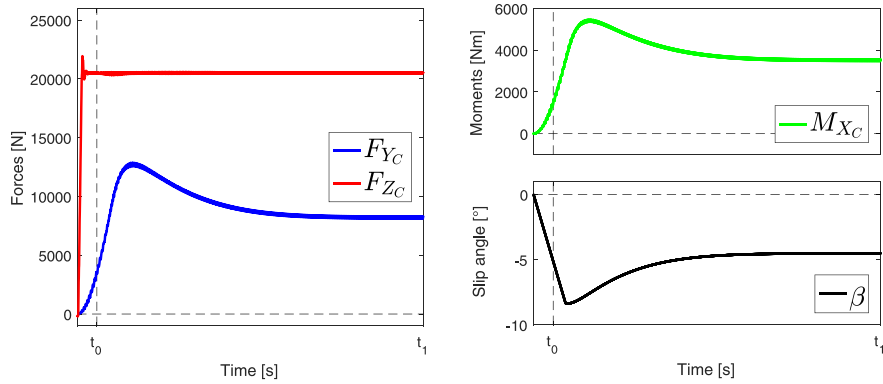
(b) RFT load case #3.
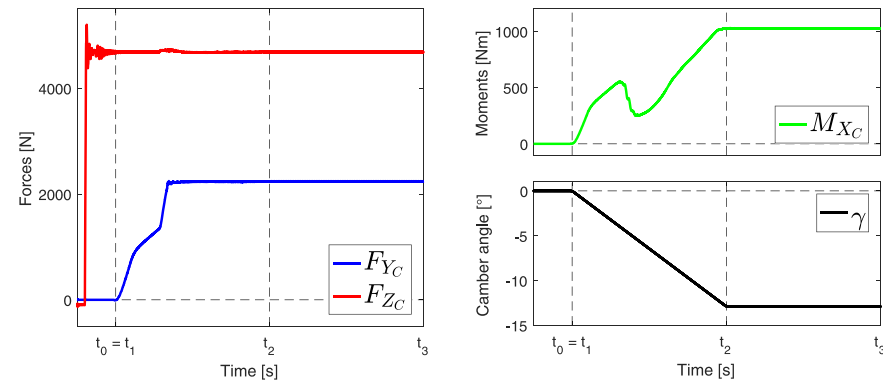
(c) BFT load case #8.

Fig. 6. CDTire WTR simulation results.

4.2. Stressed wheel

A steel wheel FE model is developed to introduce residual stresses and pre-stresses caused by manufacturing and mounting conditions. The FE model is based on 3-node and 4-node first order shell elements. Shell element formulations require less DOFs with respect to the solid counterpart i.e., 6-node and 8-node solid elements, allowing to reduce computational costs. Nevertheless, the introduction of shell elements allows a proper depiction of stress field only if curvature adjacent elements is low. Therefore, a trade-off between accuracy and computational cost depends on the limit curvature of the structure. Shell elements are suited for disc and rim components, which are obtained by forming process with large curvature radii. Lately, the stress state can be obtained by integration techniques through element thickness. The FE model simulation steps are summarised in Fig. 8.

The FE simulation is divided in five consecutive steps:

(a) RFT load case #2.

(b) RFT load case #3.

(c) BFT load case #8.
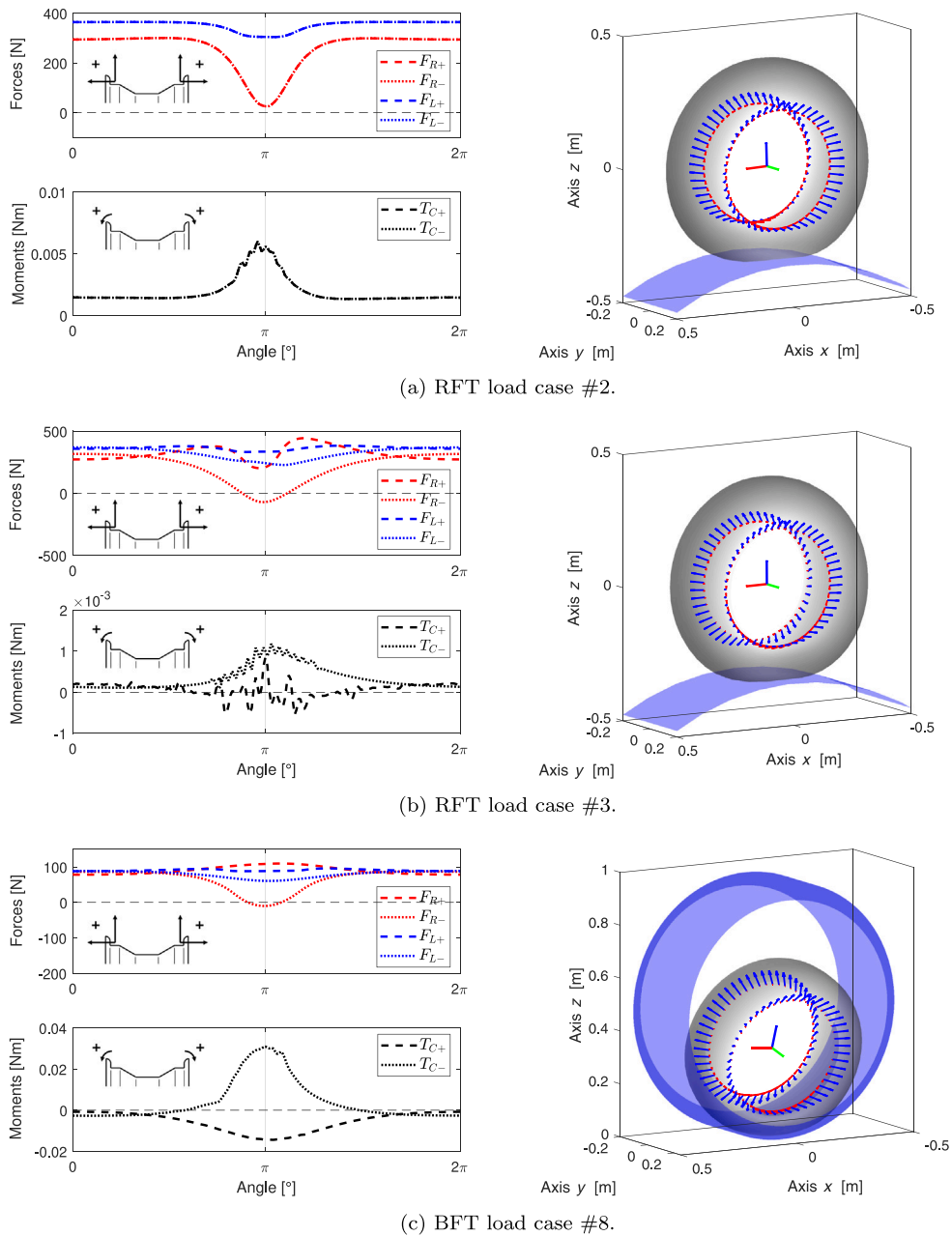
Fig. 7. CDTire WTR steady-state load profile results. Generalised force distributions on rim flanges (left) and the corresponding graphical representation (right).

- *Base state*: the wheel mesh describes the nominal size of the components, even though overclosure occurs. Constraints are imposed on rim flanges and disc hub to guarantee the press-fit assembly with the prescribed *ET* hub offset (Fig. 8a).
- *Fitting*: the initial overclosure is resolved by elastic deformation of rim channel and disc in the press-fit region. Consequently, residual stresses are introduced in the whole wheel since the constraint previously applied (Fig. 8b).
- *Disc springback*: the constraints on disc hub and are removed. Stress relief occurs in the disc nose and hub (Fig. 8c).
- *Disc clamping/Rim springback*: new constraints are applied on the disc hub while rim flange constraints are removed. Stress relief occurs in the rim flanges (Fig. 8d);
- *Bolt tightening*: the bolt hole regions are subject to concentrated forces equivalent to the tightening torque applied during mounting. The bolt hole is subject to plastic deformation (Fig. 8e). To describe the loss of tightening torque, two different steps are performed by imposing nominal and residual tightening torque measured at the end of a fatigue test. The two FE model stress states are used for cumulative damage calculation (see Section 4.4.2).
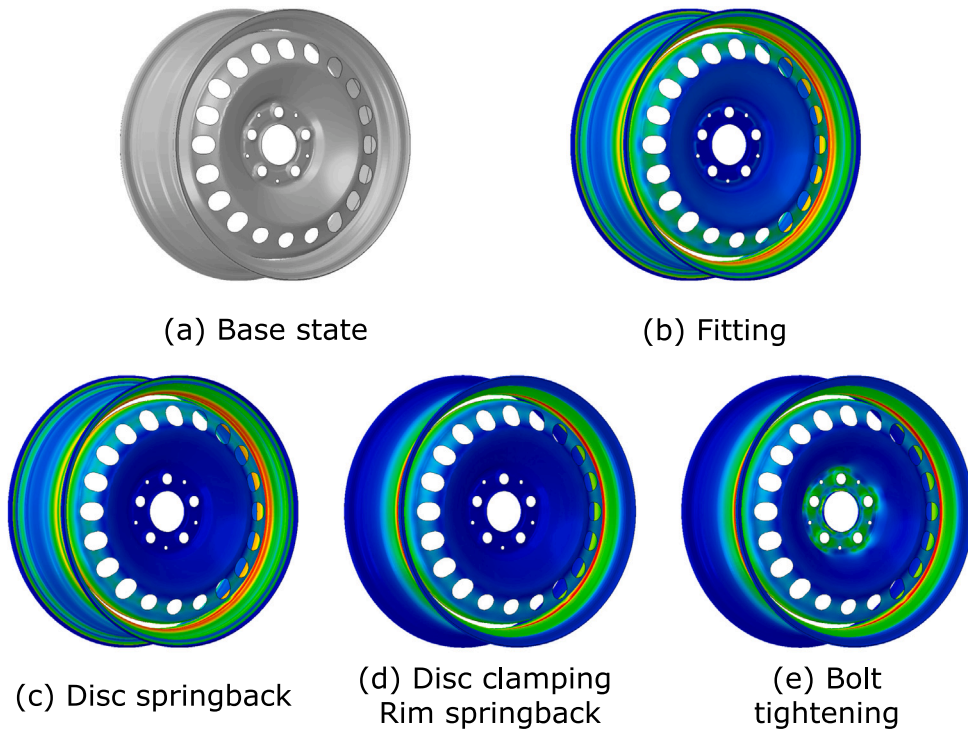
Fig. 8. Automotive steel wheel FE model simulation steps.

In the proposed case study the finite element model is developed with Abaqus. The wheel mesh is composed by shell elements of the first order S4R and S3R: the S3R elements number has been maintained under 3% of the total to reduce their stiffening contribution. The reference mesh size for disc and rim components is 4 mm. The mesh is automatically divided in components and stress coordinate system is modified to be cylindrical. The whole mesh is further prepared by identifying sensible node sets and element sets. The boundary conditions and loading conditions are always applied on the same nomenclature sets. In detail the selected sets are:

- *nset_discPlate_bc*: a set of nodes used to clamp the disc during fitting procedure; the region is extended to not affect with residual stress the hub region during fitting (Fig. 9(a));
- *nset_discPlate_contact*: a set of nodes used to hinge the disc region which is in contact with the axle hub (Fig. 9(b));
- *nset_discShaft_bc*: a set of nodes used to constraint rotational degrees of freedom of the wheel (Fig. 9(c));
- *nset_rimTyre_bc*: a set of nodes related to inner and outer flanges used to constraint the rim during fitting procedure (Fig. 9(d));
- *nset_rimTyre_load*: a set of nodes related to inner and outer flanges used to apply loads extracted from CDTire; in case of DCFT, the load is applied only on the outer flange (Fig. 9(e));
- *nset_discBH#_load*: sets of nodes related to border annular region of each bolt hole; equivalent concentrated force to fitting torque is applied on those nodes; # is substituted to an integer number for each bolt hole on the disc (Fig. 9(f));
- *eset_rimChannel_fit*: a set of rim elements involved during fitting procedure (Fig. 9(g));
- *eset_diskChannel_fit*: a set of disc elements involved during fitting procedure (Fig. 9(h)).

Further details on boundary conditions application and fitting procedure definition can be found in [38].

In this paperwork, safety welding on the rim channel is not considered in the simulation scheme, since it was not applied in the industrial case study (see Section 5).

4.3. Batch static analysis

The stressed wheel FE model is then subject to generalised force fields ($\tilde{\mathbf{F}}_w$ and $\tilde{\mathbf{T}}_w$). The loading conditions are applied on the wheel on n_w circular crown nodes per each rim flange. Therefore, the generalised reaction forces are applied from the tyre nodes to the rim flange nodes by adopting a rigid interface. A detailed description of the adopted tyre-rim rigid interface has been proposed by the authors in [14]. Typically $n_t < n_w$, therefore the concentrated generalised force fields ($\tilde{\mathbf{F}}_t$ and $\tilde{\mathbf{T}}_t$) at n_t locations are interpolated, where n_t is number of annular sections in the tyre mesh and n_w is the number of available mesh nodes in the FE model in the circumferential rim section. The interpolation is performed independently for each rim flange using the λPCH interpolation

(a) *nset_discPlate_bc*

(b) *nset_discPlate_contact*

(c) *nset_discShaft_bc*

(d) *nset_rimTyre_bc*

(e) *nset_rimTyre_load*

(f) *nset_discBH#_load*

(g) *eset_rimChannel_fit*

(h) *eset_discChannel_fit*
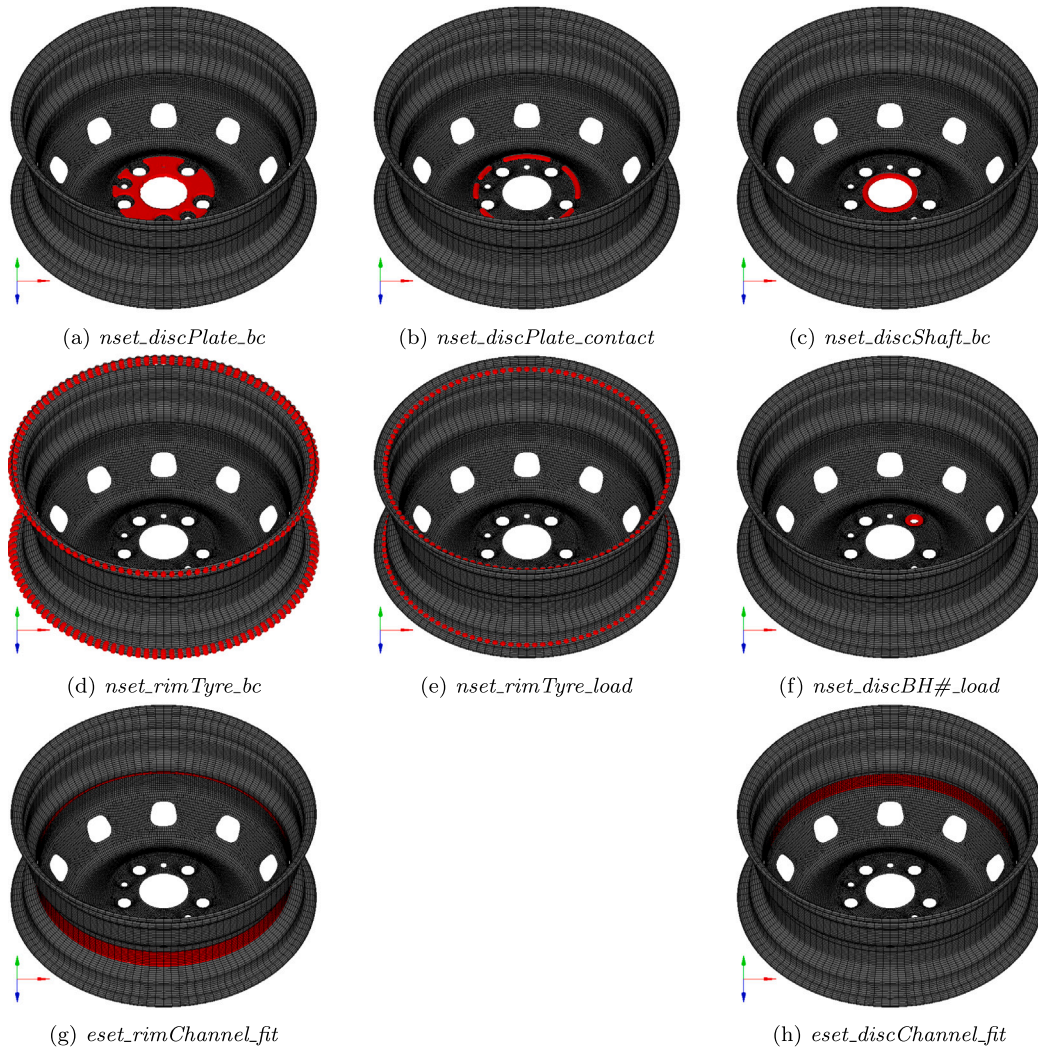
Fig. 9. Subsets defined for boundary conditions, loading conditions application.

technique, which preserves the continuity of force fields. The resulting concentrated generalised reaction fields ($\tilde{\mathbf{F}}_w$ and $\tilde{\mathbf{T}}_w$) at n_w are then scaled by the scale factor n_t/n_w. This approach converges to a distributed loading condition when $n_w \to \infty$. The application of $\tilde{\mathbf{F}}_w$ and $\tilde{\mathbf{T}}_w$ is performed on the constrained wheel FE model with n_w static analyses by rotating the generalised force fields among the wheel revolution axis of angle δ_w:

$$\delta_w = \frac{2w}{n_w}\pi \tag{4}$$

where $w = 1, \ldots, n_w$ is an integer scaling factor of a whole wheel turn. Since, rim mesh is developed by equidistant revolution of a profile, the easiest approach for load application is to shift the load profile of an angle compatible with the angular distance between two rim profiles δw. In this way, the load profile has to be rotated only, without further interpolation required. The solution is found in static regime as dynamic effect is assumed to be negligible. The result of batch static analysis is a direct stress tensor path $\boldsymbol{\sigma}(w)$ in angular domain with n_w for each element, node, and integration section of the wheel FE model.

4.4. Damage calculation

In this section the damage calculation i.e., the last step of the proposed DT architecture, is investigated. The damage calculation relies on the choices of proper failure and damage criteria. Since the wheel structure is subject only to cyclic elastic deformation, High Cycle Fatigue (HCF) criterion has been selected. Moreover, the stress tensor path is non-proportional and biaxial in the wheel regions typically affected by failure (see Appendix for further details). Therefore, a multi-axial approach has to be adopted to perform fatigue analysis. McDiarmid criterion [51,52] has been selected and properly simplified to consider the intrinsic biaxial stress state

of a FE model composed by shell elements only. Then, Palmgren–Miner cumulative damage criterion is adopted to linearly collect damage of single cycles. The damage criterion is modified to consider linear variation of mean stress, representative of loss of tightening torque phenomenon in wheel fatigue tests. Finally, this section is divided in two subsections: the first related to the reduced McDiarmid criterion development, and the second one introducing the modified Palmgren–Miner criterion.

4.4.1. Reduced mcdiarmid criterion

The McDiarmid criterion [51] assumes the critical plane is the plane where the maximum alternate tangential stress occurs. Nevertheless, the critical plane is not necessarily subject to maximum normal stress, and it is not the plane in which maximum damage occurs. The method is historically expressed as the following equation, in which failure is not occurring if the inequality is satisfied:

$$\frac{\tau_{a,\max}}{\tau_{f_{A,B}}} + \frac{\sigma_{n,\max}}{2\sigma_{UTS}} \leq 1 \tag{5}$$

where:

- $\tau_{f_{A,B}}$ is the shear fatigue limit for Irwin mode A i.e., opening due to a tensile stress normal to the plane of the crack, and Irwin mode B i.e., sliding mode due to a shear stress acting parallel to the plane of the crack and perpendicular to the crack front;
- σ_{UTS} is the ultimate tensile strength of material.
- $\tau_{a,\max}$ is the maximum alternate tangential shear;
- $\sigma_{n,\max}$ is the maximum normal stress.

The calculation of $\tau_{a,\max}$ and $\sigma_{n,\max}$ requires the identification of the critical plane by observing several layers of the direct stress tensor $\boldsymbol{\sigma}(w)$ path:

$$\boldsymbol{\sigma}(w) = \begin{bmatrix} \sigma_{xx}(w) & \tau_{xy}(w) & \tau_{xz}(w) \\ \tau_{yx}(w) & \sigma_{yy}(w) & \tau_{yz}(w) \\ \tau_{zx}(w) & \tau_{zy}(w) & \sigma_{zz}(w) \end{bmatrix} \tag{6}$$

where $w = 1, \ldots, n_w$ index refers to the wth angular position of n_w positions of tensor path after batch static analysis. $\boldsymbol{\sigma}(w)$ is evaluated in different layers n_l.

$$\boldsymbol{\sigma}_l(w) = \mathbf{R}_l^T \boldsymbol{\sigma}(w)\mathbf{R}_l \tag{7}$$

where index $l = 1, \ldots, n_l$ refers to the lth layer. The $\mathbf{R}_l$ rotation matrix rotates $\boldsymbol{\sigma}(w)$ from $\mathcal{R}(\boldsymbol{x}, \boldsymbol{y}, \boldsymbol{z})$ reference frame to the lth $\mathcal{R}(\boldsymbol{u}_l, \boldsymbol{v}_l, \boldsymbol{w}_l)$ one. The $\mathbf{R}_l$ rotation matrix is defined as:

$$\mathbf{R}_l = \begin{bmatrix} 1 & 0 & 0 \\ 0 & \cos\varphi_l & -\sin\varphi_l \\ 0 & \sin\varphi_l & \cos\varphi_l \end{bmatrix} \begin{bmatrix} \cos\theta_l & 0 & -\sin\theta_l \\ 0 & 1 & 0 \\ \sin\theta_l & 0 & \cos\theta_l \end{bmatrix} \begin{bmatrix} \cos\psi_l & -\sin\psi_l & 0 \\ \sin\psi_l & \cos\psi_l & 0 \\ 0 & 0 & 1 \end{bmatrix} \tag{8}$$

where $\varphi, \theta, \psi \in [0, \pi)$ are defined rotation matrix angles. The rotated $\boldsymbol{\sigma}_l(w)$ in $\mathcal{R}(\boldsymbol{u}_l, \boldsymbol{v}_l, \boldsymbol{w}_l)$ is structured as:

$$\boldsymbol{\sigma}_l(w) = \begin{bmatrix} \sigma_{uu}(w) & \tau_{uv}(w) & \tau_{uw}(w) \\ \tau_{vu}(w) & \sigma_{vv}(w) & \tau_{vw}(w) \\ \tau_{wu}(w) & \tau_{wv}(w) & \sigma_{ww}(w) \end{bmatrix} \tag{9}$$

The τ_{a_l} lth alternate shear is computed for each layer by inspecting all the calculated shear values $\tau_l(w)$ in angular position domain:

$$\tau_{a_l} = \frac{1}{2}\left(\max\{\tau_l(w)\} - \min\{\tau_l(w)\}\right) \tag{10}$$

Therefore, maximum alternate tangential stress $\tau_{a,\max}$ is obtained by searching the maximum in all n_l layers.

$$\tau_{a,\max} = \max\{\tau_{a_l}\} \tag{11}$$

The maximum normal stress lies in the critical plane i.e., the maximum lth layer where $\tau_{a,\max}$ occurs:

$$\sigma_{n,\max} = \max\{\sigma_l(w)\} \tag{12}$$

The canonical McDiarmid definition of maximum alternate tangential stress described in Eq. (10) depends on spherical coordinates φ, θ, and ψ. In the proposed FE application, z direction principal stress is null, hence it is possible to reduce the number of layers by passing from spherical to cylindrical layers in ψ only. Therefore, Eq. (6) becomes:

$$\boldsymbol{\sigma}(w) = \begin{bmatrix} \sigma_{xx}(w) & \tau_{xy}(w) \\ \tau_{yx}(w) & \sigma_{yy}(w) \end{bmatrix} \tag{13}$$

Also, Eq. (8) becomes:

$$\mathbf{R}_l = \begin{bmatrix} \cos\psi_l & -\sin\psi_l \\ \sin\psi_l & \cos\psi_l \end{bmatrix} \tag{14}$$

This simplification of the failure criterion strongly affects computational costs but also stress description, which is limited to three independent quantities instead of the canonical six. Nevertheless, this simplification is consistent with the FE shell element formulation in which the out-of-plane stress state is absent.

The presence of multiple shear fatigue limits for failure modes, makes the McDiarmid method quite complicated to be implemented, since the distinction in $\tau_{f_{A,B}}$ is usually not experimentally evaluated. For combined bending and torsion loads, mode A failure develops [56]. Therefore, $\tau_{f_{A,B}} = \tau_{R-1}$ where τ_{R-1} is the shear stress fatigue limit for fully reversible torsion. According to experimental and numerical evidence [56]:

- $\tau_{R-1}/\sigma_{R-1} = 1$ for extremely hard–brittle metals, and crack plane is closed to critical plane.
- $\tau_{R-1}/\sigma_{R-1} = 1/\sqrt{3}$ for brittle–ductile metals, and crack plane to critical plane angle is 45°.

Hence, Eq. (5) is rewritten in a reduced equality formulation of normalised damage factor D, anticipating the usage in the next industrial case study (Section 5) in which all the used steels show brittle–ductile behaviour:

$$D = \frac{\sqrt{3}\tau_{a,\max}}{\sigma_{R-1}} + \frac{\sigma_{n,\max}}{2\sigma_{UTS}} \tag{15}$$

The damage factor D is normalised with respect to σ_{R-1} defined as "HCF-infinite life" threshold for 2 million cycles to failure. Therefore, $D < 1$ means infinite life, and $D > 1$ means less cycles to failure than threshold. The exact N is obtained by the intersection of $\tau_{a,\max}$ and $\sigma_{n,\max}$ with the corresponding material Wöhler curve.

Actually, the calculation of number fatigue life in terms of number of cycles N occurs by intersecting the material Wöhler curve evaluated at fully reversible load and 50% of failure rate with the equivalent fully reversible alternate stress $\sigma_{a,eq}$. The $\sigma_{a,eq}$ can be computed by manipulating Eq. (15) for constant D.

$$\sigma_a = \frac{\sqrt{3}\tau_{a,\max} 2\sigma_{UTS}}{2\sigma_{UTS} - \sigma_{n,\max}} \tag{16}$$

The $\sigma_{a,eq}$ can be directly compared with material Wöhler curve without the necessity to recompute it for different value of load reversibility R. In this paperwork, the material Wöhler curves are defined for 50% of failure rate on material samples from MW Italia S.r.l characterisation.

4.4.2. Palmgren–miner criterion for mean stress variation

This section presents a developed analytical procedure to perform cumulative damage calculation on a component subject to linear varying mean stresses with cycles. The methodology is based on the Palmgren–Miner cumulative damage (PMCD) criterion for metals. The solution implies the integration of the probability density function (PDF) of the mean stress and can be extended to continuous variation with cycles.

The PMCD assumes the component damage is the linear combination of different load case contributions. Hence, linear superposition and commutative properties can be applied to damage. Therefore, the PMCD expresses the non-dimensional damage D as a summation of fractions:

$$D = \sum_i^{n_i} \frac{n_i}{N_i} \tag{17}$$

where n_i is the number of cycles applied to the component with the ith load regime, and N_i is the number of life cycles to failure at the same load regime. Also, N_i is obtainable through the simplified Wöhler curve analytical expression:

$$N_i = N \left(\frac{\sigma_{a,eq,i}}{\sigma_{R-1}} \right)^{-K} \tag{18}$$

where K is the exponential slope of simplified Wöhler curve, $\sigma_{a,eq,i}$ is the ith equivalent fully reversible stress. By substituting Eqs. (18) and (15) in Eq. (17), it is obtained the following equation:

$$D = \frac{1}{N} \sum_i^{n_i} n_i \left(1 - \frac{\sigma_{n,\max,i}}{2\sigma_{UTS}} \right)^{-K} \tag{19}$$

It is possible to describe the linear variation of $\sigma_{n,\max}$ in $n = \sum_i^{n_i} n_i$ cycles by defining its PDF. It is analysed the case of linear variation between $\sigma_{n,\max,1}$ and $\sigma_{n,\max,2}$ such as $\sigma_{n,\max,2} > \sigma_{n,\max,1}$. Therefore, the PDF is defined as:

$$p\left(\sigma_{n,\max}\right) = \frac{1}{|\sigma_{n,\max,2} - \sigma_{n,\max,1}|} = \frac{1}{\Delta\sigma_{n,\max}} \tag{20}$$

The passage to continuous domain by collecting Eq. (20) into Eq. (19) brings to:

$$D = \frac{n}{N} \frac{1}{\Delta\sigma_{n,\max}} \int_{\sigma_{n,\max,1}}^{\sigma_{n,\max,2}} \left(1 - \frac{\sigma_{n,\max,i}}{2\sigma_{UTS}} \right)^{-K} d\sigma_{n,\max} \tag{21}$$

Solving the definite integral in Eq. (21):

$$D = \frac{n}{N} \frac{2\sigma_{UTS}}{\Delta\sigma_{n,\max}} \frac{1}{K+1} \left[\left(1 - \frac{\sigma_{n,\max,1}}{2\sigma_{UTS}} \right)^{-K} - \left(1 - \frac{\sigma_{n,\max,2}}{2\sigma_{UTS}} \right)^{-K} \right] \tag{22}$$

In conclusion, an analytical description of Palmgren–Miner rule for linear mean stress variation is obtained. The supplied method is developed for reduced McDiarmid criterion, but the procedure is generally independent failure criteria but strongly affected by PDF in finding open form solution. The solution allows computing life of various situations such loss of tightening torque, which can be described as a linear decay of mean stress component.

4.4.3. Summary

In this section, a concise summary of the sequential steps for the damage calculation are supplied:

- Static batch analysis to obtain direct stress tensor evolution $\boldsymbol{\sigma}(w)$
- Calculation of $\tau_{a,\max}$ and $\sigma_{n,\max}$.
- Computation of damage factor D by McDiarmid method.
- Calculation of equivalent alternate stress in fully reversible condition σ_a.
- Intersection with Wöhler curve.

5. Industrial case study

In this section, an industrial case study is presented in order to validate the developed DT features. The developed DT is validated against a wide experimental fatigue test database for DCFT, RFT, and BFT load cases with different wheel topologies, characteristics and loading conditions. All the wheel geometries, material properties, and experimental data are supplied by MW Italia S.r.l.

The supplied experimental data consists of elastic material properties, engineering and true Stress–Strain ($\sigma - \varepsilon$) curves, and simplified Wöhler curves for HCF and extended for very HCF up to 1 billion cycles.

Table 2 lists the material characteristics: Young moduli E, yield strength σ_Y and ultimate tensile strength σ_{UTS}. Poisson's ratio is assumed to be always 0.3. In the whole activity, all the components are build with a dual-phase steel, and three types of High Strength Low Alloy (HSLA) steels.

Fig. 10 shows the two sets of σ-ε curves for all the wheel materials included in the presented industrial case study. The true σ-ε curves are reduced to 10 values during the elasto-plastic static analysis.

Fig. 11 shows the simplified Wöhler curves of the previous materials. The supplied Wöhler curves are simplifications fitted on experimental tests performed on calibrated specimens. The curves are defined for 50% of probability and for fully recursive load cycles $R - 1$. The alternate stress limit σ_{R-1} is supplied for $N = 2e6$. All the curves are based on the following relationship:

$$\frac{N_i}{N_{i+1}} = \left(\frac{\sigma_i}{\sigma_{i+1}} \right)^{-K} \tag{23}$$

where σ_i and σ_{i+1} are fatigue limits conditions respectively at N_i and N_{i+1} number of cycles, and K is the slope coefficient. It is important to notice $N_i < N_{i+1}$ and $\sigma_i > \sigma_{i+1}$. The HCF and vHCF segments are computed using $N_1 = 1e3$, $N_2 = 2e6$, and $N_3 = 1e9$.

The proposed experimental fatigue database spans different wheel geometries with nominal dimensions. In Table 3, all the wheels under study are listed, where n_b is the number of bolt holes, t is the laminate thickness, which spans in a range if the component is obtained by flow-forming process, and p is the nominal inflating pressure during experimental tests. In "Style" column of Table 3, the disc and the rim components are colour coded as the adopted material properties defined in Figs. 10 and 11. All the discs are developed with DP-600 material, a dual-phase steel. Instead, the rims are developed using three HSLA steel grades: HSLA-280, HSLA-360, and HSLA-480. From a macroscopic point of view, two families of automotive steel wheel geometries are studied: standard wheels ("AX" and "BX" wheels) and semi-full-face wheels ("CX" wheels). The main difference is the vent hole arrangements. Moreover, B1 is a spare wheel with a tight channel. All the wheels have double hump rim design i.e., "H2" in all wheel markings. Specifically, the selected wheel geometries allow to verify fatigue assessment sensitivity to some geometry specification variation. In detail:

- A5.1 and A5.2 shares the same disc but A5.2 rim thickness is higher.
- C1.1 and C1.2 shares the whole geometry but C1.2 offset ET is higher.
- C2.1 and C2.2 shares the same disc but C2.2 rim width is higher.

In the supplied experimental fatigue database different geometries, loading conditions and requirements in fatigue life are present. The experimental fatigue database consists of spreadsheets with recorded fatigue tests: for each experimental test, the mounting condition, the number of cycles recorded, and the crack nature are listed. Moreover, the experimental fatigue database for DCFT also includes information about nominal tightening torque, measured during the mounting procedure, and the residual tightening torque, measured at the end of the experimental test. Finally, [5%, 50%, 95%] confidence levels are extrapolated by fitting Weibull distribution to the experimental fatigue database for each loading condition.

The adopted CDTire/3D tyre models have $n_t = 50$. Instead, the wheel FE models are developed in the ABAQUS 6.20 environment using S3R and S4R shell elements. The S3R number of elements has been maintained under 3% of the total number of elements since its intrinsic stiff behaviour. All the wheel models are simplified; air valve and scallop features are absent if not stated differently. Moreover, the wheel mesh size is about 2 mm and $n_t = 104$, compromising h-convergence and computational costs for this application, and smooth interpolation of applied generalised force fields.

The reduced McDiarmid and the modified Palmgren–Miner cumulative damage criteria are implemented and computed in LUPOS [57], an open-source calculation toolbox developed in Matlab.

Table 2
Material properties.

| Material	HSLA-280	HSLA-360	HSLA-480	DP-600
E [GPa]	203	146	203	210
σ_Y [MPa]	302	371	468	368
σ_{UTS} [MPa]	383	480	522	610
σ_{R-1} [MPa]	120	140	157	190
K_{HCF} [–]		4.63		
K_{vHCF} [–]		10		
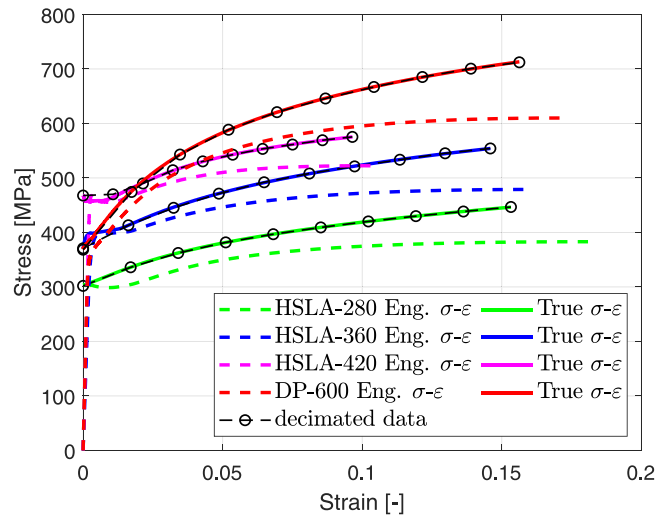
Fig. 10. Material stress–strain curves.
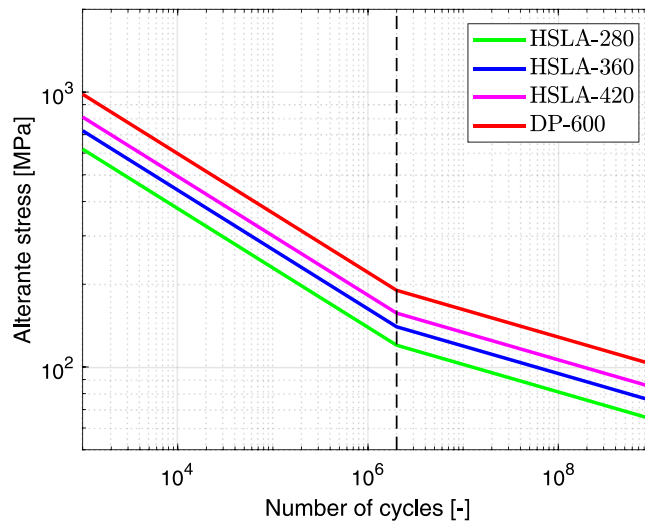
Fig. 11. Simplified Wöhler curves.

5.1. Dynamic cornering fatigue tests

In the experimental activities performed, an INMESS RBT machine is used (Fig. 12). The machine can impose a maximum dynamic cornering moment M_{DC} of 8000 N m with rotating eccentric mass. The tests are performed at 2400 rpm, excitation frequency far from first natural frequency of the clamped wheel. The machine stops when a 20% variation from rated deflection is measured. When this condition occurs, the wheel suffered fatigue, and its stiffness is reduced. Therefore, the arm deformation increases. The DCFT experimental activity is stored in a database of $10 \div 30$ trials per load case in which the test is interrupted when

Table 3
Wheel and corresponding tyre characteristics.

Wheel			Disc			Rim		Tyre	
ID	Dimensions	Style	ET [mm]	n_b [–]	t [mm]	Material	t [mm]	Dimensions	p [Pa]
A1	6J×15		39	5	3.15	HSLA-280	2.15	185/65 R15	3×10^5
A2	6J×16		68	5	4.6	HSLA-280	3.1	255/75 R16	5×10^5
A3	6J×16		36.5	5	3.3	HSLA-480	2.15	205/55 R16	3×10^5
A4	6.5×17		38	5	4.4	HSLA-480	2.2	215/60 R17	4.5×10^5
A5.1	6.5J×16		39	5	3	HSLA-480	2.325	205/55 R16	3×10^5
A5.2	6.5J×16		39	5	3	HSLA-480	2.45	205/55 R16	3×10^5
B1	4J×18		27.5	5	4.6	HSLA-360	2.0	145/80 R18	4.5×10^5
C1.1	6J×15		30	4	5.4	HSLA-360	1.5 ÷ 2.3	185/65 R15	3×10^5
C1.2	6J×15		35	4	5.4	HSLA-360	1.5 ÷ 2.3	185/65 R15	3×10^5
C2.1	6J×16		23	4	6	HSLA-280	1.4 ÷ 2.2	215/60 R16	4×10^5
C2.2	6.5J×16		20	4	6	HSLA-280	1.35 ÷ 2.2	205/55 R16	3.5×10^5
C3	6J×16		40	4	6.4	HSLA-280	2.15	195/65 R16	4.5×10^5
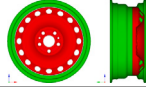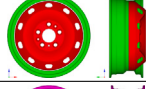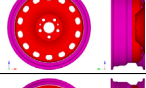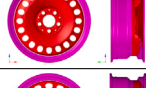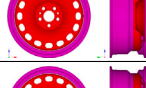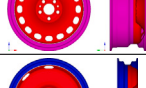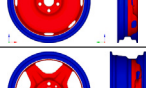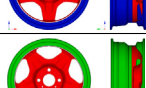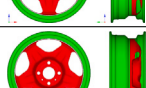
fatigue failure occurred. The database also contains the photographic documentation of typical failures, and text descriptions of each trial failure, usually occurring on the attachment face to nut seat in circumferential direction, or on the disc nose in circumferential direction. In standards, the DCFT is still quite common and consolidated technique approached by many manufacturers. The DCFT mainly forces bolt hole fatigue failure mechanisms.

Table 4 lists the different load cases experimentally tested. For each load case, the initial and the residual average bolt tightening torque T_{b0} and T_{b1} are measured. Moreover, the minimum number of cycles to failure N_{rW} requirement is supplied. The load cases have been selected to verify some expected properties:

- the singular load case sets [1, 2], [3, 4, 5], and [11, 12] are applied to the same wheel geometry with increasing M_{DC}; it is expected a reduction in fatigue life.
- load case set [6, 7] use the same M_{DC}, but applied on the same wheel geometry with different rim thickness t_{rim}; it is expected an increase in fatigue life.
- load case set [9, 10] use the same M_{DC}, but applied on the same wheel geometry with different ET; it is not expected a significant variation in fatigue life.

S. Venturini et al.

Engineering Failure Analysis 158 (2024) 107979

Fig. 12. INMESS RBT test bench.

Table 4
DCFT load cases.

Load case	Wheel ID	M_{DC} [N m]	T_{b_0} [N m]	T_{b_1} [N m]	N_{r_W} [–]
1	A1	2357	110	99.6	2.0e4
2	A1	2560	110	96.9	2.0e4
3	A2	4220	160	120	6.0e5
4	A2	5420	160	123	1.5e5
5	A2	6330	160	145.3	6.0e5
6	A5.1	2286	110	103.7	2.0e5
7	A5.2	2286	110	99.5	2.0e5
8	B1	1758	120	98.0	2.0e5
9	C1.1	1818	120	99.4	3.0e4
10	C1.2	1857	120	92.7	3.0e4
11	C3	1685	100	94	2.0e5
12	C3	2160	100	90	2.0e5

The results of the numerical simulations are compared with experimental confidence levels and minimum fatigue life requirements in Fig. 13. In the figure, the black box plot represent the Weibull confidence levels based on experimental database. The central box is the 50% of failure, while the top and bottom horizontal segments are the 5% and 95% failure confidence level. The grey boxes are the N_{r_W} requirements. Perhaps, some of the load cases experimentally shows a lower fatigue life with respect to the expected from the manufacturer i.e., load cases #3, #4, #5, #8, #11, and #12 related to wheels A2, B1, and C3. The red box plots are the DT predictions: the top and bottom horizontal segments identifies the equivalent life for T_{b_0} and T_{b_1} based simulations, while the central box is obtained by applying Eq. (22) for linear variation of maximum stress caused by the reduction of bolt tightening torque.

The DT prediction is significantly aligned with the 50% experimental failure confidence level, therefore the nominal wheel property uncertainties are centred with respect to the failure. Only load cases #6 and #7, related to A5.1-A5.2 wheels show a conservative estimation still internal the confidence levels. The DT predictions follow the expected fatigue life trends previously supposed, therefore also load case #6 and #7 results are consistent. Moreover, the DT predictions show the reduced range of variability caused by including or not the bolt tightening torque variation in the prediction. The Palmgren–Miner based DT result is bounded between best (T_{b_0}) and worst (T_{b_1}) case scenarios variability, which is proportional to the T_b variation. This result indicates the tightening torque variation could be of interest in DT prediction when $(T_{b_1} - T_{b_0})/T_{b_1}$ is larger than 10%.

Fig. 14 shows the numerical–experimental comparison of damage of most significant load cases. On the left hand side figures, it is shown the damage DF map of the inner surfaces, most critical for DCFT. On the right hand side figures, are shown the experimental failures of some samples. On light coloured surface regions (small DF) no damage is occurring, while on darker areas (large DF) the damage is higher and the fatigue life is reduced.

A red circle is depicting the most critical location on the wheel surface. Due the wheel geometry circumferential modularity, the identified most critical locations also coincide with circumferential similar regions where failure may statistically occur. In all the three load cases the crack nucleation sites are identified and are comparable with experimental evidence.

19
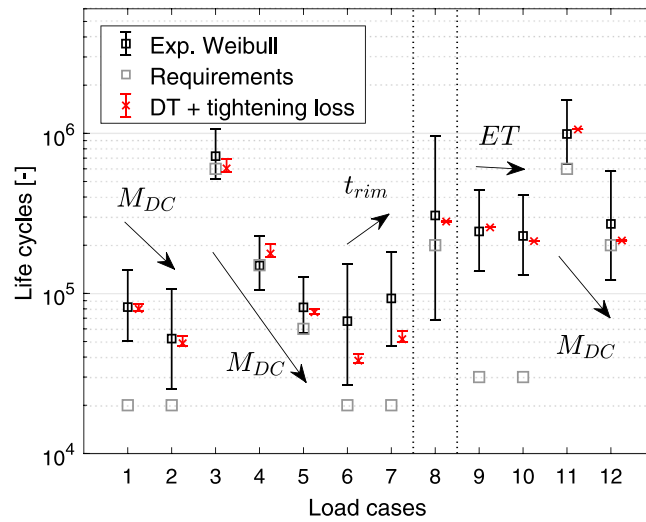
Fig. 13. DCFT numerical to experimental life cycle comparison.

Table 5
RFT load cases.

Load case	Wheel ID	F_{Z_C} [N]	F_{Y_C} [N]	β [°]	N_{r_W} [−]
1*	A1	11 330	4532	−4.2	3.3e5
2*	A2	20 500	8200	−4.5	3.3e5
3*	A2	24 280	0	0	5.0e5
4*	A3	10 500	4200	−3.5	3.3e5
5*	A5.1	10 300	4170	−3.0	3.3e5
6*	A5.2	10 300	4120	−3.1	3.3e5
7*	B1	10 673	0	0	5.0e5
8	C1.1	10 150	0	0	1.0e6
9	C1.2	10 150	0	0	1.0e6
10	C2.1	10 732	0	0	6.0e5
11	C2.2	11 478	0	0	6.0e5

5.2. Radial fatigue tests

In this validation section, RFT are performed with a Leonardo SCRFT machine (Fig. 15). The machine can apply a maximum vertical load F_{Z_C} =50 kN and a maximum lateral load F_{Y_C} =20 kN at maximum tangential speed of 130 km/h. The diameter of the drum is 1.7 m. The machine stops when the load cell in the hub measures a deviation from the reference of 10%: a crack initiation occurred on the wheel on the disc nose in radial direction to the vent holes, or on the rim channel in circumferential direction, causing sudden inflation pressure loss. In both cases, wheel radial stiffness decreases. The RFT experimental activity is stored in a database of 25 ÷ 45 trials per load case. Similarly to DCFT, the tests are usually interrupted when fatigue failure occurred i.e., the test censorship is not applied. Also, the textual indications about crack nucleation site is available for each trial, while photographic documentation is supplied for typical failures.

Table 5 list the load cases experimentally tested in this campaign. Each load case includes the slip angle β which allows the prescription of vertical and lateral loads F_{Z_C} and F_{Y_C}. The proposed load case selection allows to verify some expected properties:

- the load case set [2, 3] use decreasing F_{Y_C}, but applied on the same wheel geometry; it is expected an increase in fatigue life.
- load case set [5, 6] use the similar load, but applied on the same wheel geometry with different rim thickness t_{rim}; it is expected an increase in fatigue life.
- load case set [8, 9] use the same F_{Z_C}, but applied on the same wheel geometry with different rim thickness ET; it is not expected a significant variation in fatigue life.
- load case set [10, 11] use similar load, but applied on the same wheel geometry with different rim channel c_{rim}; it is not expected a significant variation in fatigue life.

Moreover, the load cases marked by "*" are tested against the presence of disc scallop feature in geometry.

The scallop is a peculiar geometrical feature of the discs of standard steel wheels due to manufacturing process. The standard steel wheel disc is manufactured starting from an octagonal metal sheet which is gradually formed to final shape. The forming process causes the plastic deformation of octagonal shape borders to present four inlet regions, called scallops. The presence of
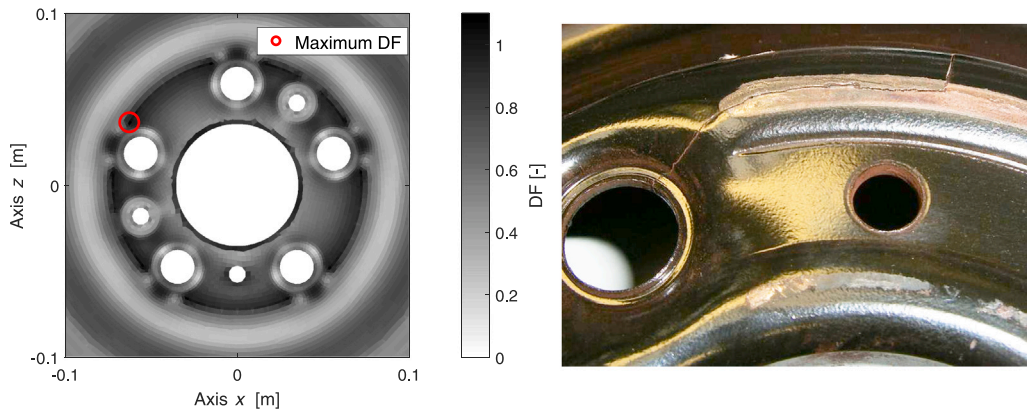
(a) Load case #4. Failure on attachment face to nut seat in circumferential direction.
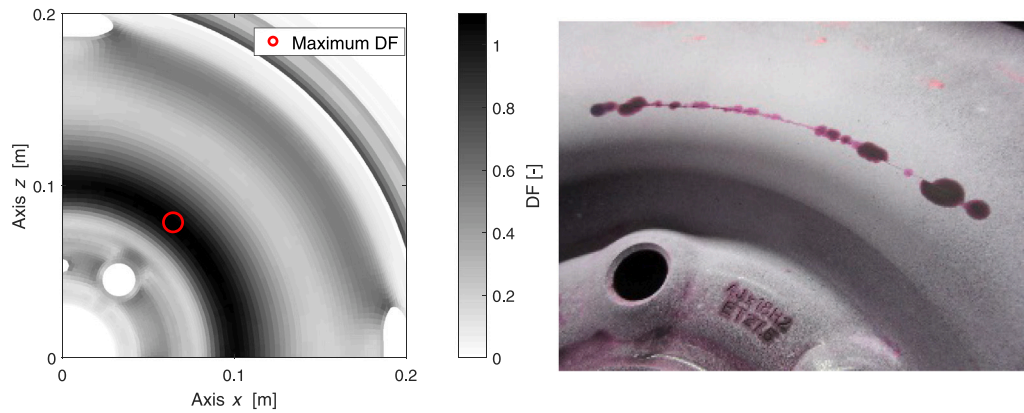
(b) Load case #8. Failure on the disc nose in circumferential direction.
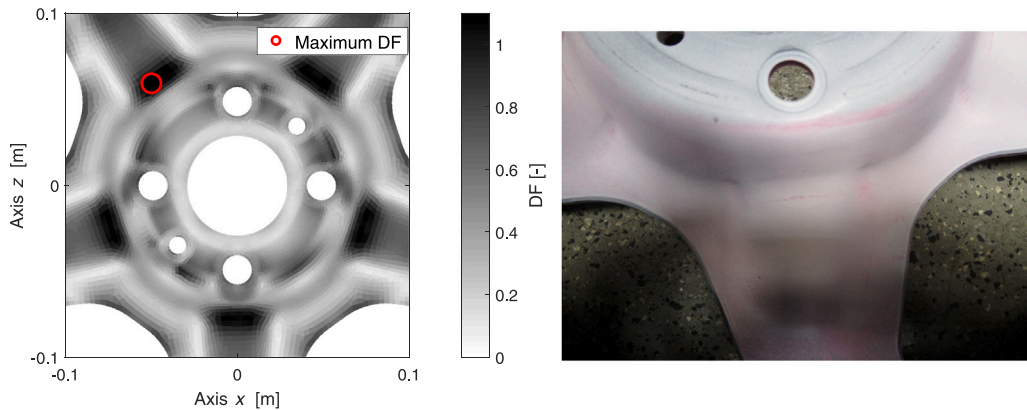
(c) Load case #10. Failure on the disc nose in circumferential direction.

Fig. 14. DCFT numerical to experimental damage comparison.

those scallops induces a stress concentration which may be crucial for wheel fatigue life on the rim channel. Therefore, the wheel FE models are modified to include scallop feature. Fig. 16 shows three examples of wheel disc modified meshes.

Fig. 17 shows the numerical to experimental comparison of DT predictions as a DT feature analysis. Similarly to Section 5.1, the black box plot represent Weibull confidence levels fitted to experimental RFT database, and the grey boxes are N_{r_W} fatigue minimum requirements. The blue "+" marks are DT predictions in which the wheel FE model has not been stressed. The wheel FE model is used in the DT in its base state using rigid links on the interference fit region between disc and rim components. The red

**Fig. 15.** Leonardo SCRFT test bench.
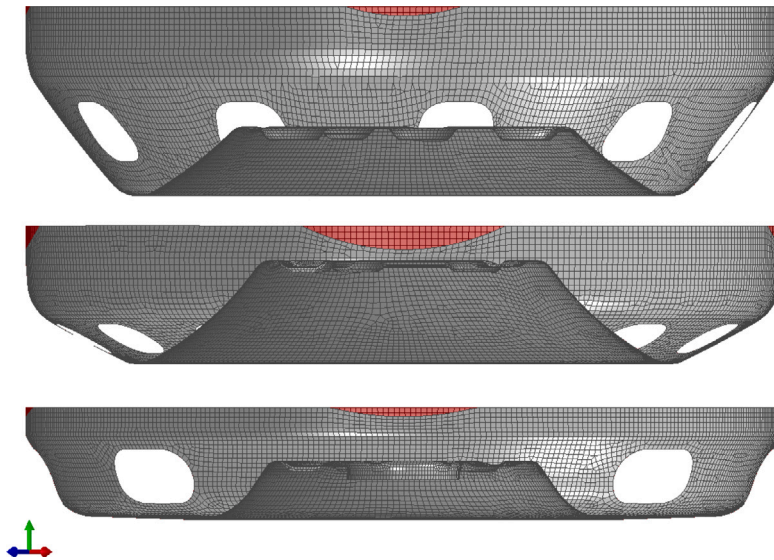
Fig. 16. Disc scallop feature: A2 (top), A3 (middle), and B1 (bottom) wheels.

"×" marks refers to original DT predictions on stressed FE wheel models. Finally, the black circles show DT predictions on stressed FE wheel models with scallop feature.

Differently from DCFT, fatigue minimum requirements are non aligned with Weibull confidence levels, hence wheels tend to fail before minimum cycle requirements. The comparison between DT predictions with and without stressed FE wheel models is evident. Specifically, the application of residual and pre-stresses is crucial in load cases #7 to #11 i.e., spare standard wheels and semi-full-face wheels. Instead, the role of scallop is conservative in DT prediction. With respect to scallop examples in Fig. 16 the effect is more significant when failure occurs on rim channel i.e., load cases #2, #3, and #7 with A2 and B1 wheels. The scallop presence strongly reduces component fatigue life from about 33% up to 50%.

Globally, the results are more scattered than DCFT. The full DT predictions are included in Weibull confidence levels but not for load cases #2 to #3. The fact the results are not centred in confidence levels as minimum requirements let the authors suppose manufacturing and/or testing biases are present in the experimental database. Also, expected trends for the selected tests are qualitatively described. While loading conditions trend are well kept i.e., load cases #2 and #3, geometrical feature expected trends are less defined. Fig. 18 shows the numerical–experimental comparison of damage of most significant load cases. On the left hand side figures, it is shown the damage DF map of the wheel surfaces most critical for RFT.

In all the three load cases the crack nucleation sites are identified and are comparable with experimental evidence of some samples on the right hand side.
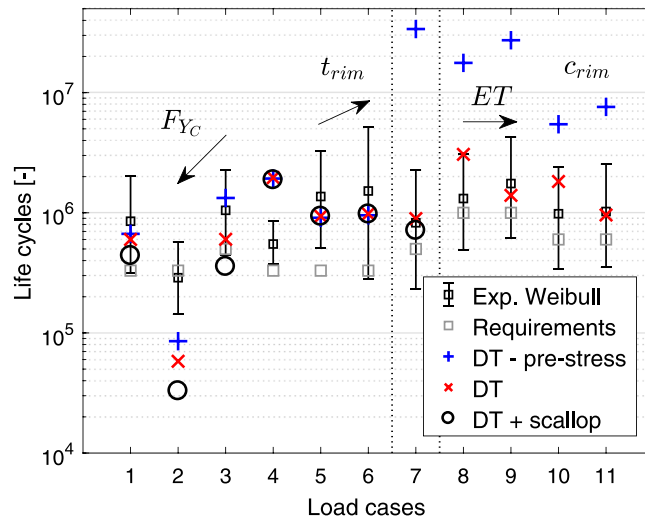
**Fig. 17.** RFT numerical to experimental life cycle comparison.

Table 6
BFT load cases.

| Load case	Sequences	F_{Z_C} [N]	F_{Y_C} [N]	γ_{OTM} [°]	N_{r_W} [–]
1	15, 31	15 944	−8392	14.0	318
2	23, 25	2 822	−1353	9.1	604
3	27, 29	3 837	−1150	6.8	669
4	7, 9, 11, 13, 19, 21	5 079	0	0.8	655
5	5	10 722	0	0.2	318
6	1, 3	4 232	203	−1.2	734
7	30, 32	4 345	1353	−9.3	586
8	26	4 684	2232	−12.9	577
9	22	5 982	3382	−13.9	343
10	24	8 239	3450	−11.8	206
11	18	6 772	4194	−15.3	200
12	20	5 869	4532	−18.5	200
13	16	7 167	5615	−18.5	242
14	12	8 860	5682	−17.3	190
15	10	10 158	5682	−16.9	227
16	4	10 209	6580	−18.5	138
17	8	8 465	6765	−18.5	206
18	6	9 368	7170	−18.5	249
19	14, 28	15 944	8392	−18.5	318
20	2	11 978	8984	−18.5	117

5.3. Biaxial fatigue tests

The adopted machine is an MTS 855 [55] (Fig. 19), identified by SAE J2562 as an option C biaxial. The MTS 855 measures tyre reactions directly through two load cells mounted on the extremities of a rotating hub: the rotation of the camber angle γ allows to pass from a parallel axis condition, mono-axial, to a biaxial state. Before the BFT load cases are conducted, experimental OTM procedure is performed to identify the necessary camber angle for each loading condition. In this paperwork, the γ_{OTM} are experimentally evaluated. Nevertheless, the authors developed a fully automated OTM procedure implemented in a previous version of DT dedicated to BTF study [14].

The experimental BFT campaign is based on the OEM standard AK-349 procedure. This procedure requires a set of 167 repetitions of the whole load program. Table 6 shows the load cases based on 33 non-unique redacted sequences after OTM and the simplifications applied in order to perform the DT prediction:

- The nominal bolt tightening torque is 130 N m for all the loading conditions.
- Drum speed is reduced to 88.6 rpm to ensure enough stress field samples for fatigue assessment; this is possible since in steady-state conditions.
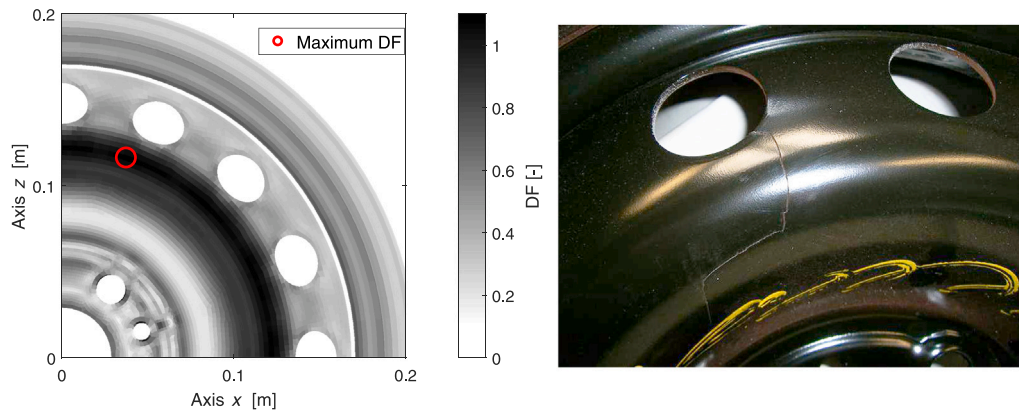
(a) Load case #1. Failure on the disc nose to the vent holes in radial direction (outer surface).
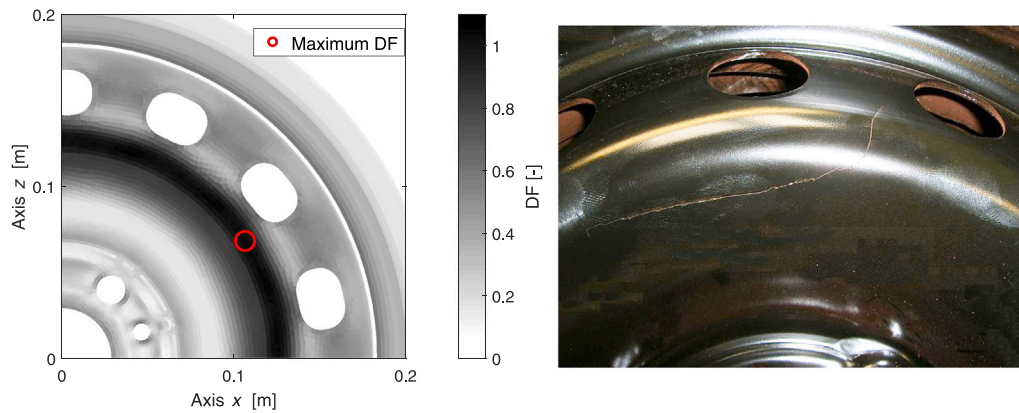
(b) Load case #4. Failure on the disc nose to the vent holes in radial direction (outer surface).
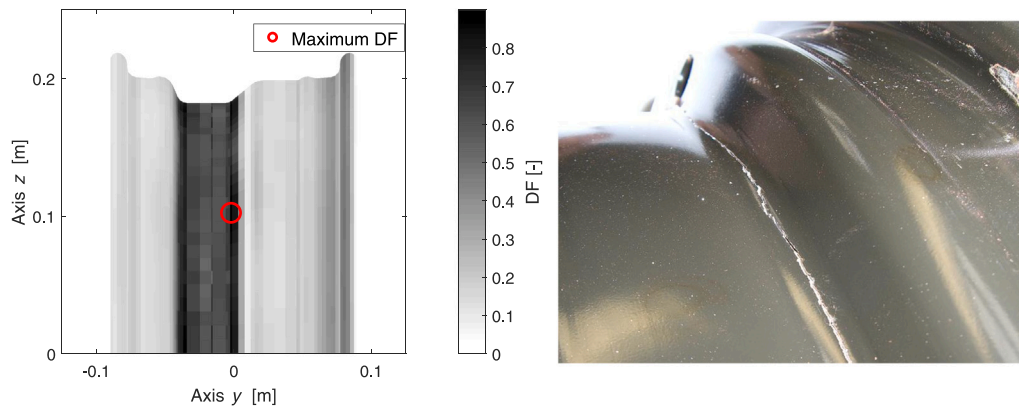
(c) Load case #10. Failure on the rim channel in circumferential direction (inner surface).

Fig. 18. RFT numerical to experimental damage comparison.

- Load cases #1 and #19 have different experimental camber angle amplitudes but this difference is not perceivable by WTR results, since rigid wheel is used.
- Load cases #4 and #5, since they have null lateral load, generates in WTR null camber angles; this behaviour is not physical since the experimental flexibility of the rim.

Fig. 19. BFT MTS 855 test bench [55].

Table 7
BFT results. Numerical to experimental comparison.

Configuration	Cycles [–]	Completion [%]	Failure
(a) (Experimental)	623 515	26.2	Nose radially to vent hole (Fig. 21(a) right)
(a) (Numerical)	653 360	27.4	Nose (Fig. 21(a) left)
(b) (Experimental)	1 211 401	51	Rim channel (Fig. 21(b) right)

The experimental activity is performed on A4 steel wheel model (see Table 3). The wheel is not flow-formed and presents an anomalous geometry on 3 vent holes in order to dynamically balance the presence of the air valve. The experimental campaign is performed on two different configurations:

- *Configuration (a)*: A4 steel wheel from normal production.
- *Configuration (b)*: A4 with reworked vent holes, obtained by manual filing, no extra knowledge.

Fig. 20 shows the DT non cumulative prediction of each load case on the fatigue assessment: on the ordinate are listed all the unique load cases (20) while on the abscissa the ratio between the ratio of the required number of cycles with a certain load case to obtain failure on the requested number of cycles requested by the load program for all the required repetitions in the whole load program.

If the ratio is greater than 1 (vertical black dashed dot line at 10^0) the load cycle contribution is not sufficient to induce the wheel failure by itself and is less significant. From Fig. 20 it is possible to see that load case #19 is the most critical for both the disc and the rim components. In the figure, are shown in red and blue lines the load case contributions on rim and disc surfaces. The fatigue failure is going to occur on the inner disc surface before the rim inner surface.

The DT non cumulative prediction identifies the most significant load case in BFT. The further application of Palmgren–Miner rule allows to identify the most critical regions for fatigue life requirements. Table 7 shows the experimental and numerical cumulative results, of the two configurations. The DT cumulative prediction allows to estimate the configuration (a) failure with 1.2% of underestimation. Moreover, by looking at the damage maps in Fig. 21, also the configuration (b) failure is qualitatively predicted.

Fig. 21(a) shows the normal production wheel fatigue failure starts from the vent hole and propagates in radial direction to the nearest bolt hole. Instead, Fig. 21(b) shows the failure of the reworked wheel sample: it occurs on the channel in circumferential direction, causing the wheel to lose inflating pressure. Since the most critical load case participation on the rim is almost double than the disc, also the failure at the rim channel is estimated. In this second case, the fatigue life of the wheel is almost doubled, as experimentally observed. A confirm of this result can be seen in the DT prediction, in which the damage map is critical in the nose region connection to vent holes with damage factor 1.85 but also in the channel region where the damage factor is 1.6.

In conclusion, the main and secondary fatigue failure can be predicted by the proposed DT by applying Palmgren–Miner rule.
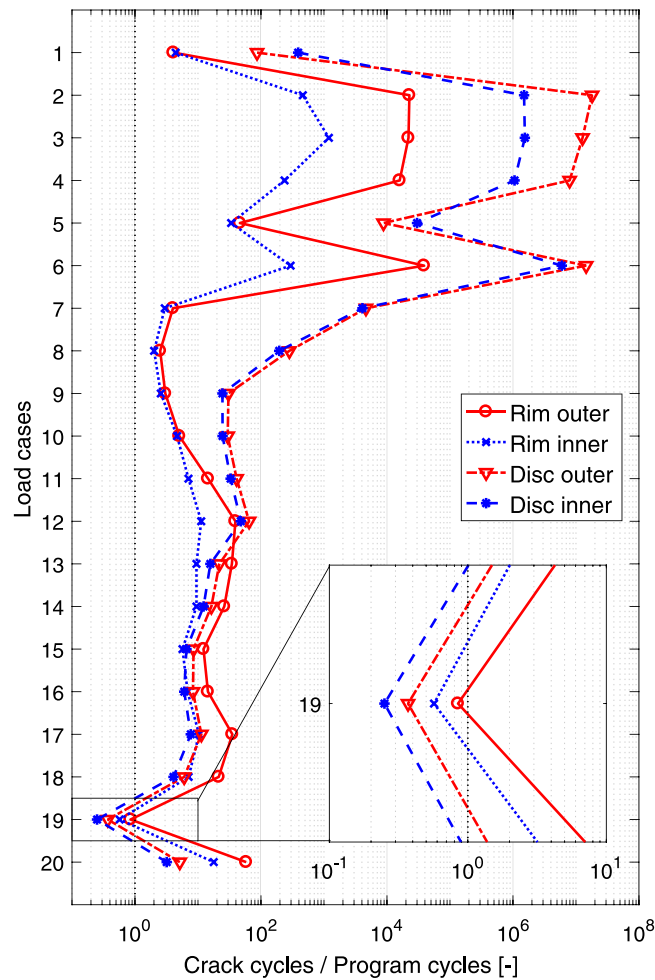
Fig. 20. A4 wheel BFT non-cumulative damage ratio.

6. Conclusions

In this paper, a DT of automotive steel wheel for accelerated fatigue tests is developed, discussed, and validated by comparison with a wide experimental database of fatigue failures in different fatigue tests i.e., DCFT, RFT, and BFT.

The proposed DT architecture allows to exploit decoupled tyre-rim rigid interface developed in a preliminary DT model in [14] to perform fatigue life prediction on a wide range of testing procedures, loading conditions, and wheel topologies. The tyre and wheel decoupled simulations with different boundary conditions have been deeply validated, showing the effectiveness of the assumptions for wheel design process.

The approach is capable to identify the crack nucleation sites and quantify the fatigue life according to the material life specifications. The DT has been tested for uncertainty quantification by comparing the predictions with Weibull failure distributions based on experimental data.

Secondly, DT effective functionality has been tested by comparing the full DT prediction with non stressed wheel case. It has been demonstrated how the residual stress and pre-stress mechanisms are fundamental DT features to obtain significant results. In the next steps, a further experimental activity will be performed to map residual stress evolution on disc and rim components during forming processes.

Also, geometrical wheel features as disc scallop, and uncertainty in bolt tightening torque are considered. It is demonstrated the effectiveness of the developed DT architecture for automotive steel wheel manufacturer design process. The DT enables design optimisation and reduction of costs associated with prototyping and experimental testing during the development phase.

In the future, the DT architecture will be improved to allow fast multi-parameter uncertainty quantification. Also, some features must be improved or investigated. The residual stress induced by forming process on both disc and rim components will be introduced, both as an additional simulation step and mean stress distribution on the wheel. Moreover, the tyre-rim rigid interface will be improved to reduce the introduced assumptions: it is expected an improved rim flange pressure distribution, which implies
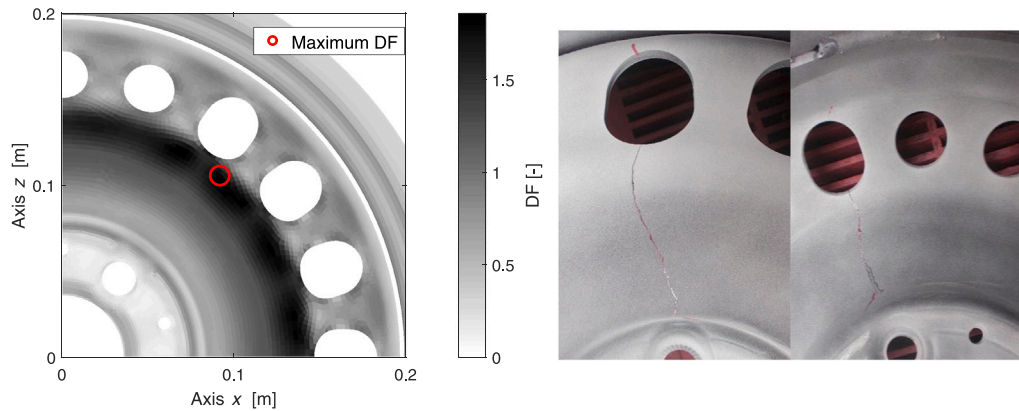
(a) Normal production. Failure on the disc nose to the vent holes in radial direction (inner surface).
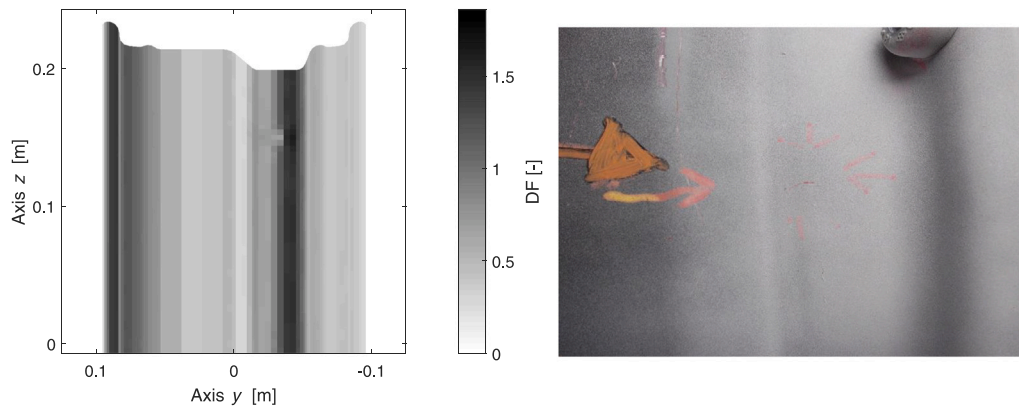
(b) Reworked vent holes. Failure on the rim channel in circumferential direction (inner surface).

Fig. 21. BFT numerical to experimental damage comparison.

the passage to a stiff interface and interactive DT model. Finally, it is in our plan to extend the whole DT architecture to more generalised loading conditions for real-time health monitoring.

CRediT authorship contribution statement

Simone Venturini: Writing – review & editing, Writing – original draft, Validation, Software, Methodology, Investigation, Formal analysis, Data curation, Conceptualization. **Carlo Rosso:** Supervision, Software, Resources, Project administration, Methodology, Investigation, Conceptualization. **Mauro Velardocchia:** Supervision, Software, Resources, Project administration, Funding acquisition.

Declaration of competing interest

The authors declare that they have no known competing financial interests or personal relationships that could have appeared to influence the work reported in this paper.

Data availability

The data that has been used is confidential.
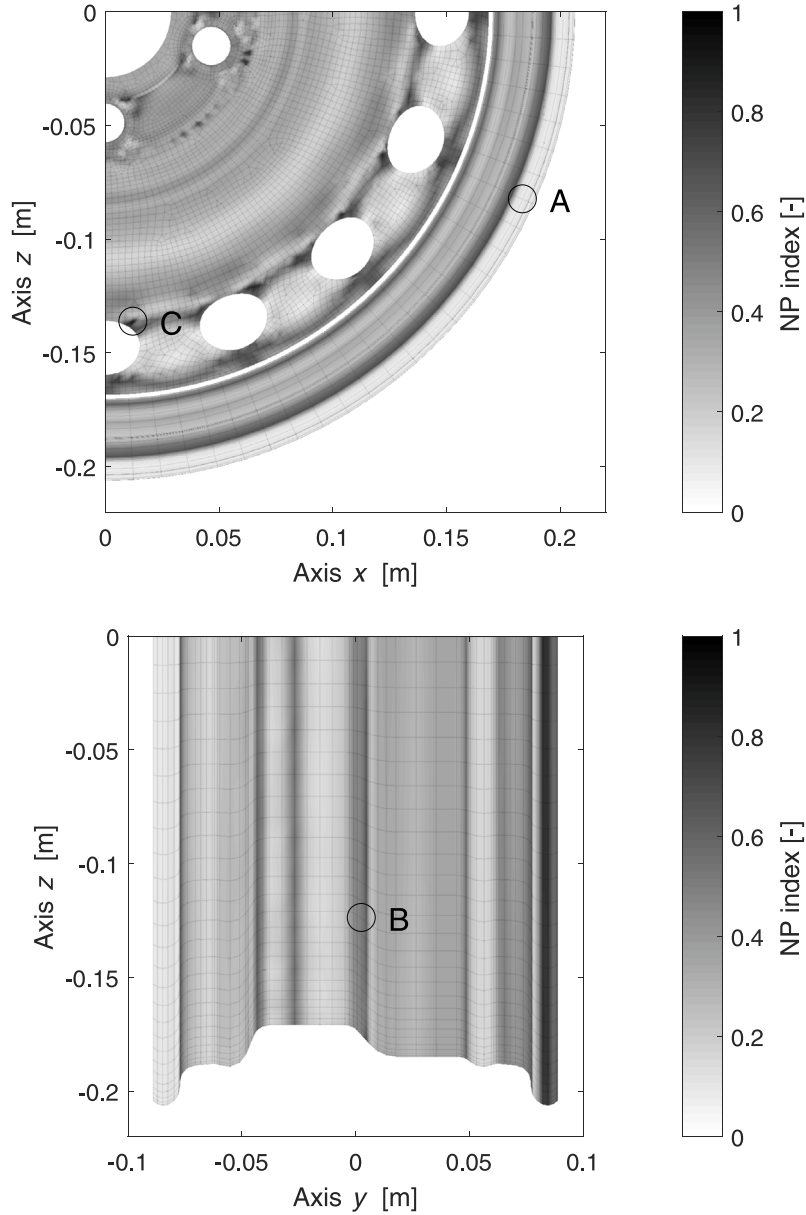
Fig. A.22. NPi applied to RFT load case #11: inner surface (top) and outer surface (bottom).

Appendix. Identification of non-proportionality in multi-axial stress path

It is suspected the automotive steel wheels under generic loading conditions, locally present a stress tensor path which is non-proportional, asynchronous and aperiodic. The proofs of stress path non-proportionality and multi-axiality are necessary for failure criterion selection. Therefore, a basic methodology based on FE simulation is described to depict the overall non-proportionality and multi-axiality in stress path.

A direct Cauchy stress tensor in the wth position of its path $\boldsymbol{\sigma}(w)$ presents three principal stress components $\sigma_1(w)$, $\sigma_2(w)$, and $\sigma_3(w)$. In our specific application, the direct stress tensor is always biaxial by definition, hence one of the principal stresses is null. By focusing on the two non-null principal stress paths, now σ_1 and σ_2, it is possible to describe the principal stress tensor path with an equivalent ellipsoidal path. The equivalent ellipsoidal path is found by solving the eigen-problem on the covariance matrix C:

$$C = k \begin{bmatrix} \mathrm{cov}(\bar{\boldsymbol{\sigma}}_1, \bar{\boldsymbol{\sigma}}_1) & \mathrm{cov}(\bar{\boldsymbol{\sigma}}_1, \bar{\boldsymbol{\sigma}}_2) \\ \mathrm{cov}(\bar{\boldsymbol{\sigma}}_2, \bar{\boldsymbol{\sigma}}_1) & \mathrm{cov}(\bar{\boldsymbol{\sigma}}_2, \bar{\boldsymbol{\sigma}}_2) \end{bmatrix} \tag{A.1}$$
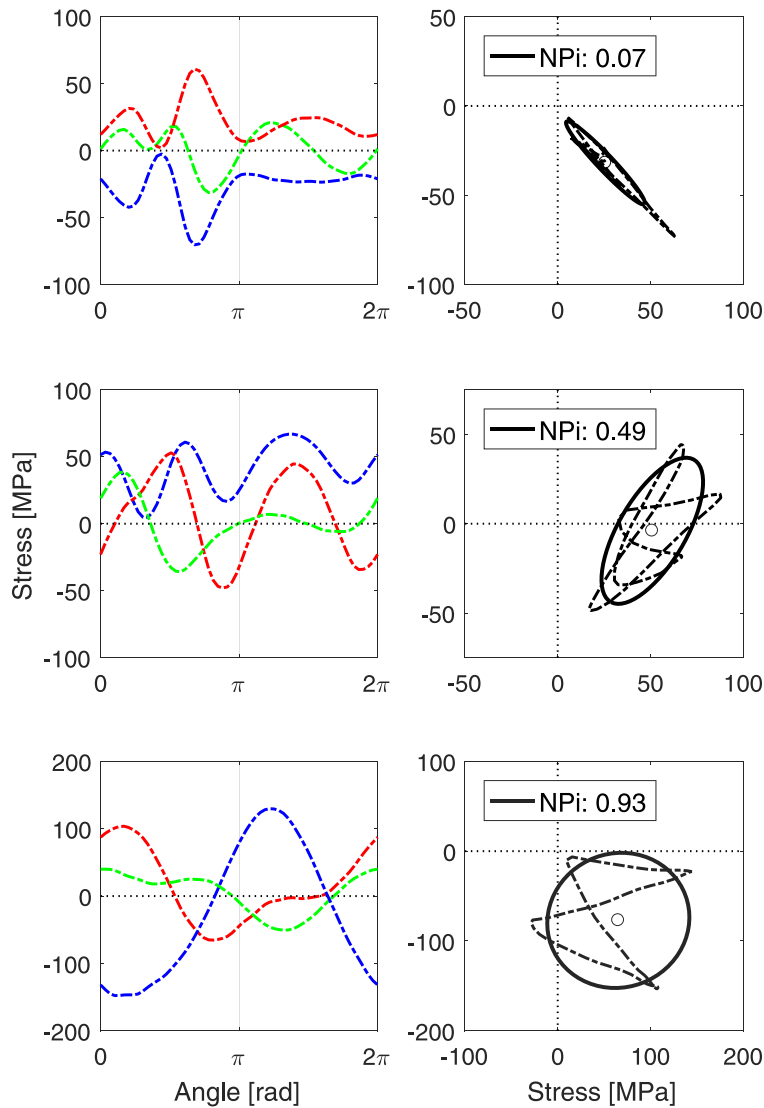
Fig. A.23. NPi details: almost proportional stress path (top), very non-proportional stress path (bottom).

where k is the χ-square inverse cumulative function value for a given probability, $\bar{\sigma}_1$ and $\bar{\sigma}_2$ are the principal stress paths epurated from mean values μ_1 and μ_2. The resulting eigenvalues a and b represent the semi-axis lengths with $a \geq b$, while the corresponding eigenvectors $\boldsymbol{V}_a$ and $\boldsymbol{V}_b$ represent their directions in the σ_1-σ_2 plane. The NPi non-proportionality and multi-axiality index is thereby composed:

$$\text{NPi} = \frac{1}{2}\left(\frac{b}{a} + (1 - |\boldsymbol{\mu} \cdot \boldsymbol{V}_a|)\right) \tag{A.2}$$

where $\boldsymbol{\mu} = \{\mu_1, \mu_1\}^T$ identifies the ellipsoidal path centroid.

The ratio between semi-axis a and b is an index of significance of principal stress components, e.g., $b/a = 1$ is obtained when the fitted ellipse is circular and both principal stress components are equally contributing to state of stress, while $b/a = 0$ is obtained when the fitted ellipse is degenerate into a straight line, i.e., principal stress components are in-phase or out-of-phase, therefore the state of stress is mono-axial. Instead, the second term is related to non-proportionality of the greater principal stress. If $|\boldsymbol{\mu} \cdot \boldsymbol{V}_a| = 0$, the greater principal stress is orthogonal to the centroid arm, therefore, even if the state of stress is mono-axial, the behaviour is non-proportional. Instead, if $|\boldsymbol{\mu} \cdot \boldsymbol{V}_a| = 1$ the two vectors are parallel, therefore, the state of stress is proportional.

The methodology is applied on the RFT load case #11 (see Table 5) using probability of 95% of samples fitting. The application of the index is graphically shown in Fig. A.22. The NPi is higher in darker regions, while it is absent on lighter ones.

Fig. A.23 helps to visualise the NP index computed at specific FE model locations A, B, and C indicated by black circles in Fig. A.22. On the left side, the three direct stress tensor paths are represented: in red σ_{xx}, in blue σ_{yy}, and in green τ_{xy}. On the right

side, the principal stress path is depicted and the fitted ellipsoidal path with corresponding NPi index. Despite the limited region affected by load, the effect is perceivable on the rest of the geometry. The non-proportional behaviour is limited to the loaded zones where fitting, bolt tightening and tyre interactions occur.

The first two graphs are related to wheel rim locations *A* at outer rim flange, and *B* at interference region section. The *A* section presents a NPi = 0.07, the equivalent ellipse is compact and the principal stresses are almost proportional. Instead, the *B* section presents a NPi = 0.49, in which both non-proportionality and multi-axiality are consistent.

Finally, the last graph is related to *C* disc vent hole location. At this location NPi = 0.91, and the equivalent ellipsoidal path is almost circular, and definitely non-proportional behaviour occurs. The observation of the evolution of principal stresses shows that they are definitely non-proportional i.e., the maximum stress is not always located in the same plane, therefore it is not possible to apply traditional yield criteria. It is evident that a multi-axial non-proportional failure criterion is necessary.

References

[1] G. Leister, Passenger Car Tires and Wheels: Development — Manufacturing — Application, Springer International Publishing, 2018.

[2] M. Guiggiani, The Science of Vehicle Dynamics: Handling, Braking, and Ride of Road and Race Cars, Springer International Publishing, 2018.

[3] Y. Nakajima, Advanced Tire Mechanics, Springer Singapore, 2019.

[4] ISO 3894:2023 Road vehicles — Wheels/rims for commercial vehicles — Test methods, 2023.

[5] ETRTO — European Tyre and Rim Technical Organisation, Standards manual 2020, 2020.

[6] Wheel Standards Committee, SAE J328 Wheels — Passenger car and light truck performance requirements and test procedures, 2021, http://dx.doi.org/10.4271/J328_202107.

[7] Wheel Standards Committee, SAE J2562 Biaxial wheel fatigue test, 2021, http://dx.doi.org/10.4271/J2562_202107.

[8] Association of European Wheel Manufacturers, EUWA ES-3.23 biaxial fatigue test for trucks wheels, 2017.

[9] E. Bonisoli, A.D. Vella, S. Venturini, Uncertainty effects on bike spoke wheel modal behaviour, Conf. Proc. Soc. Exp. Mech. Ser. (2023) 111–123, http://dx.doi.org/10.1007/978-3-031-04090-0_13.

[10] S. Venturini, E. Bonisoli, C. Rosso, D. Rovarino, M. Velardocchia, Modal analyses and meta-models for fatigue assessment of automotive steel wheels, Conf. Proc. Soc. Exp. Mech. Ser. (2020) 155–163, http://dx.doi.org/10.1007/978-3-030-47638-0_17.

[11] M. Grieves, Digital Twin: Manufacturing Excellence Through Virtual Factory Replication, White paper, 2014.

[12] M. Grieves, J. Vickers, Digital twin: Mitigating unpredictable, undesirable emergent behavior in complex systems, in: Transdisciplinary Perspectives on Complex Systems, 2017, pp. 85–113.

[13] C. Semeraro, M. Lezoche, H. Panetto, M. Dassisti, Digital Twin paradigm: A systematic literature review, Comput. Ind. 130 (2021) 103469, http://dx.doi.org/10.1016/j.compind.2021.103469.

[14] S. Venturini, E. Bonisoli, C. Rosso, M. Velardocchia, A tyre-rim interaction digital twin for biaxial loading conditions, Mech. Mach. Theory 191 (2024) http://dx.doi.org/10.1016/j.mechmachtheory.2023.105491.

[15] S.K. Pal, D. Mishra, A. Pal, S. Dutta, D. Chakravarty, S. Pal, Digital Twin – Fundamental Concepts to Applications in Advanced Manufacturing, Springer Cham, 2022, p. 465, http://dx.doi.org/10.1007/978-3-030-81815-9.

[16] F. Biesinger, B. Kraß, M. Weyrich, A survey on the necessity for a digital twin of production in the automotive industry, in: 2019 23rd International Conference on Mechatronics Technology, ICMT, 2019, pp. 1–8, http://dx.doi.org/10.1109/ICMECT.2019.8932144.

[17] M. Dal Borgo, S.J. Elliott, M. Ghandchi Tehrani, I.M. Stothers, Virtual sensing of wheel position in ground-steering systems for aircraft using digital twins, in: Z. Mao (Ed.), Model Validation and Uncertainty Quantification, Volume 3, Springer International Publishing, Cham, 2020, pp. 107–118, http://dx.doi.org/10.1007/978-3-030-47638-0_12.

[18] A.J. Zakrajsek, S. Mall, The development and use of a digital twin model for tire touchdown health monitoring, in: 58th AIAA/ASCE/AHS/ASC Structures, Structural Dynamics, and Materials Conference, 2017, pp. 1–16, http://dx.doi.org/10.2514/6.2017-0863.

[19] M.A. de Menezes Lourenço, J.J. Eckert, F.L. Silva, M.H.R. Miranda, L.C. de Alkmin e Silva, Uncertainty analysis of vehicle fuel consumption in twin-roller chassis dynamometer experiments and simulation models, Mech. Mach. Theory 180 (2023) 105126, http://dx.doi.org/10.1016/j.mechmachtheory.2022.105126.

[20] P. Gardner, M. Dal Borgo, V. Ruffini, Y. Zhu, A. Hughes, Towards the development of a digital twin for structural dynamics applications, in: Z. Mao (Ed.), Model Validation and Uncertainty Quantification, Volume 3, Springer International Publishing, Cham, 2020, pp. 165–179, http://dx.doi.org/10.1007/978-3-030-47638-0_18.

[21] J. Yu, Y. Song, D. Tang, J. Dai, A Digital Twin approach based on nonparametric Bayesian network for complex system health monitoring, J. Manuf. Syst. 58 (2021) 293–304, http://dx.doi.org/10.1016/j.jmsy.2020.07.005.

[22] S. Venkatesan, K. Manickavasagam, N. Tengenkai, N. Vijayalakshmi, Health monitoring and prognosis of electric vehicle motor using intelligent-digital twin, IET Electr. Power Appl. 13 (9) (2019) 1328–1335, http://dx.doi.org/10.1049/iet-epa.2018.5732.

[23] R.S. Magargle, L. Johnson, P. Mandloi, P. Davoudabadi, O. Kesarkar, S. Krishnaswamy, J. Batteh, A. Pitchaikani, A simulation-based digital twin for model-driven health monitoring and predictive maintenance of an automotive braking system, in: Proceedings of the 12th International Modelica Conference, Linköping University Electronic Press, 2017, pp. 35–46, http://dx.doi.org/10.3384/ecp1713235.

[24] P.K. Rajesh, N. Manikandan, C.S. Ramshankar, T. Vishwanathan, C. Sathishkumar, Digital twin of an automotive brake pad for predictive maintenance, Procedia Comput. Sci. 165 (2019) 18–24, http://dx.doi.org/10.1016/j.procs.2020.01.061.

[25] C. Cappellini, L. Giorleo, G. Allegri, A. Attanasio, E. Ceretti, A digital twin approach to automotive wheel flow forming process, in: D.T. Matt, R. Vidoni, E. Rauch, P. Dallasega (Eds.), Managing and Implementing the Digital Transformation, Springer International Publishing, Cham, 2022, pp. 114–126, http://dx.doi.org/10.1007/978-3-031-14317-5_10.

[26] H. Pacejka, I.J. Besselink, Tire and Vehicle Dynamics, in: Electronic Publications, Elsevier Science, 2012.

[27] F. Ballo, G. Previati, M. Gobbi, G. Mastinu, A semi-analytical tyre model for the study of tyre/rim interaction on a road vehicle, in: International Design Engineering Technical Conferences and Computers and Information in Engineering Conference, Vol. Volume 3: 19th International Conference on Advanced Vehicle Technologies; 14th International Conference on Design Education; 10th Frontiers in Biomedical Devices, 2017, pp. 1–12, http://dx.doi.org/10.1115/DETC2017-67730.

[28] F. Ballo, G. Previati, M. Gobbi, G. Mastinu, Tire-rim interaction, a semi-analytical tire model, J. Mech. Des. 140 (4) (2018) http://dx.doi.org/10.1115/1.4038927.

[29] M. Gipser, FTire – the tire simulation model for all applications related to vehicle dynamics, Veh. Syst. Dyn. 45 (sup1) (2007) 139–151, http://dx.doi.org/10.1080/00423110801899960.

[30] cosin scientific software AG, FTire/rim - Extension to FTire/core for flexible and visco-plastic rim modelling, 2022.

[31] B. Manfred, G. Axel, R. Michael, Noise, vibration, harshness model of a rotating tyre, Veh. Syst. Dyn. 54 (4) (2016) 474–491, http://dx.doi.org/10.1080/00423114.2016.1158844.

[32] M. Roller, P. Betsch, A. Gallrein, J. Linn, An enhanced tire model for dynamic simulation based on geometrically exact shells, Arch. Mech. Eng. 63 (2) (2016) 277–295, http://dx.doi.org/10.1515/meceng-2016-0016.

[33] Stress & Strength GmbH, LBF®.WheelStrength - Numerical analysis of the structural durability of rotating chassis components, 2022.

[34] D. Kong, D.-Z. Sun, B. Yang, H. Qiao, C. Wei, Y. Lang, H. Song, J. Gao, Characterization and modeling of damage behavior of a casting aluminum wheel considering inhomogeneity of microstructure and microdefects, Eng. Fail. Anal. 145 (2023) 107018, http://dx.doi.org/10.1016/j.engfailanal.2022.107018.

[35] Y.-C. Duan, F.-F. Zhang, D. Yao, J.-H. Hu, R. Dong, X. Zhao, Y.-P. Guan, Multiscale fatigue-prediction method to assess life of A356-T6 alloy wheel under biaxial loads, Eng. Fail. Anal. 130 (2021) 105752, http://dx.doi.org/10.1016/j.engfailanal.2021.105752.

[36] A. Mazzoni, L. Solazzi, Experimental field test on a multipiece steel wheel and influence of the material properties on its fatigue life evaluation, Eng. Fail. Anal. 135 (2022) 106106, http://dx.doi.org/10.1016/j.engfailanal.2022.106106.

[37] S.B. Koppisetti, R. Nallu, R.R. Penmetsa, Passenger cars wheel performance test simulation for service life evaluation: A review, J. Fail. Anal. Prev. 22 (4) (2022) 1370–1392, http://dx.doi.org/10.1007/s11668-022-01447-0.

[38] D. Rovarino, L. Actis Comino, E. Bonisoli, C. Rosso, S. Venturini, M. Velardocchia, M. Baecker, A. Gallrein, Hardware and Virtual Test-Rigs for Automotive Steel Wheels Design, SAE Technical Papers 2020, http://dx.doi.org/10.4271/2020-01-1231.

[39] Z.-G. Zheng, T. Sun, X.-Y. Xu, S.-Q. Pan, S. Yuan, Numerical simulation of steel wheel dynamic cornering fatigue test, Eng. Fail. Anal. 39 (2014) 124–134, http://dx.doi.org/10.1016/j.engfailanal.2014.01.021.

[40] D. Shang, X. Liu, Y. Shan, E. Jiang, Research on the stamping residual stress of steel wheel disc and its effect on the fatigue life of wheel, Int. J. Fatigue 93 (2016) 173–183, http://dx.doi.org/10.1016/j.ijfatigue.2016.08.020.

[41] Y. Zhao, M. Ma, R. Qin, Y. Ling, G. Wang, X. Wan, H. Gu, Y. Liu, A fabrication history based strain-fatigue model for prediction of crack initiation in a radial loading wheel, Fatigue Fract. Eng. Mater. Struct. 40 (11) (2017) 1882–1892, http://dx.doi.org/10.1111/ffe.12607.

[42] X. Wan, Y. Shan, X. Liu, T. He, J. Wang, Tire-rim interface pressure of a commercial vehicle wheel under radial loads: theory and experiment, Meas. Sci. Technol. 28 (11) (2017) http://dx.doi.org/10.1088/1361-6501/aa8895.

[43] D. Rovarino, L. Actis Comino, E. Bonisoli, C. Rosso, S. Venturini, M. Velardocchia, M. Baecker, A. Gallrein, A Methodology for Automotive Steel Wheel Life Assessment, SAE Technical Papers 2020-April, 2020, http://dx.doi.org/10.4271/2020-01-1240.

[44] M. Zanchini, D. Longhi, S. Mantovani, F. Puglisi, M. Giacalone, Fatigue and failure analysis of aluminium and composite automotive wheel rims: Experimental and numerical investigation, Eng. Fail. Anal. 146 (107064) (2023) http://dx.doi.org/10.1016/j.engfailanal.2023.107064.

[45] F.M. Santiciolli, R. Möller, I. Krause, F.G. Dedini, Simulation of the scenario of the biaxial wheel fatigue test, Adv. Eng. Softw. 114 (2017) 337–347, http://dx.doi.org/10.1016/j.advengsoft.2017.08.006.

[46] X. Wan, Y. Shan, X. Liu, H. Wang, J. Wang, Simulation of biaxial wheel test and fatigue life estimation considering the influence of tire and wheel camber, Adv. Eng. Softw. 92 (2016) 57–64, http://dx.doi.org/10.1016/j.advengsoft.2015.11.005.

[47] F. Ballo, G. Mastinu, G. Previati, M. Gobbi, Numerical modelling of the biaxial fatigue test of aluminium wheels, in: International Design Engineering Technical Conferences and Computers and Information in Engineering Conference, Vol. 4: 22nd International Conference on Advanced Vehicle Technologies (AVT), 2020, http://dx.doi.org/10.1115/DETC2020-22142, V004T04A018.

[48] K. Reza Kashyzadeh, G. Farrahi, Improvement of HCF life of automotive safety components considering a novel design of wheel alignment based on a Hybrid multibody dynamic, finite element, and data mining techniques, Eng. Fail. Anal. 143 (2023) 106932, http://dx.doi.org/10.1016/j.engfailanal.2022.106932.

[49] M. Cima, L. Solazzi, Experimental and analytical study of random fatigue, in time and frequencies domain, on an industrial wheel, Eng. Fail. Anal. 120 (2021) 105029, http://dx.doi.org/10.1016/j.engfailanal.2020.105029.

[50] M. Marco Antonio, d. Jaime Tupiassú Pinho, An improved multiaxial rainflow algorithm for non-proportional stress or strain histories – Part I: Enclosing surface methods, Int. J. Fatigue 42 (2012) 217–226, http://dx.doi.org/10.1016/j.ijfatigue.2011.10.014.

[51] D. McDiarmid, A shear stress based critical-plane criterion of multiaxial fatigue failure for design and life prediction, Fatigue Fract. Eng. Mater. Struct. 17 (12) (1994) 1475–1484, http://dx.doi.org/10.1111/j.1460-2695.1994.tb00789.x.

[52] D. Socie, G. Marquis, Multiaxial Fatigue, SAE International, 1999.

[53] ISO 3911:2021 Wheels and rims for pneumatic tyres — Vocabulary, designation and marking, 2021.

[54] J.J.M. van Oosten, H.-J. Unrau, A. Riedel, E. Bakker, Standardization in tire modeling and tire testing—TYDEX workgroup, TIME project, Tire Sci. Technol. 27 (3) (1999) 188–202, http://dx.doi.org/10.2346/1.2135984.

[55] MTS Systems Corporation, Panoramica sul funzionamento Sistema di prova del carico di fatica multiassiale per ruote serie 855, 2015.

[56] A. Carpinteri, A. Spagnoli, Multiaxial high-cycle fatigue criterion for hard metals, Int. J. Fatigue 23 (2) (2001) 135–145, http://dx.doi.org/10.1016/S0142-1123(00)00075-X.

[57] E. Bonisoli, L. Dimauro, S. Venturini, LUPOS: Open-source scientific computing in structural dynamics, Conf. Proc. Soc. Exp. Mech. Ser. (2023) 177–188, http://dx.doi.org/10.1007/978-3-031-34946-1_23.